AXISYMMETRIC RADIATIVE TITANIUM DIOXIDE MAGNETIC NANOFLUID FLOW ON A STRETCHING CYLINDER WITH HOMOGENEOUS/ HETEROGENEOUS REACTIONS IN DARCY-FORCHHEIMER POROUS MEDIA: *INTELLIGENT NANOCOATING SIMULATION*

P.K. Pattnaik[1], S. R. Mishra[2*], O. Anwar Bég[3], Umar F. Khan [4] and J.C. Umavathi[5]

[1]*Department of Mathematics, College of Engineering Technology, Bhubaneswar, **India.***
[2]*Department of Mathematics, Siksha 'O' Anusandhan Deemed to be University, Bhubaneswar, Odisha 751030, **India***.
[3]*Professor and Director - Multi-Physical Engineering Sciences Group (MPESG), Department of Mechanical/Aeronautical Engineering, SEE, University of Salford, Manchester, **UK***.

[4] *Electromagnetics Research, School of Engineering, Robert Gordon University, Aberdeen, **Scotland***.

[5] *Visiting Professor, Dipartimento di Ingegneria, Università degli Studi della Campania "Luigi Vanvitelli", Aversa, **Italy.***

***Corresponding author- email:** satyaranjan_mshr@yahoo.co.in*
Co-author emails: papun.pattnaik@gmail.com; O.A.Beg@salford.ac.uk; u.khan@rgu.ac.uk ;
drumavathi@rediffmail.com

ABSTRACT:

Modern nanomaterials coating processes feature high temperature environments and complex chemical reactions required for the precise synthesis of bespoke designs. Such flow processes are extremely complex and feature both heat and mass transfer in addition to viscous behaviour. Intelligent nano-coatings exploit magnetic nanoparticles and can be manipulated by external magnetic fields. Mathematical models provide an inexpensive insight into the inherent characteristics of such coating dynamics processes. Motivated by this, in the current work, a novel mathematical model is developed for dual catalytic reactive species diffusion in axisymmetric coating enrobing forced convection boundary layer flow from a linearly axially stretching horizontal cylinder immersed in a homogenous non-Darcy porous medium saturated with magnetic nanofluid. Homogeneous and heterogeneous reactions, heat source (e.g. laser source) and non-linear radiative transfer are included. The Tiwari-Das nanoscale model is deployed. A Darcy-Forchheimer drag force formulation is utilized to simulate both bulk porous drag and second order inertial drag of the porous medium fibres. The magnetic nanofluid is an aqueous electroconductive polymer comprising base fluid water and magnetic TiO_2 nanoparticles. The TiO_2 nanoparticles are one chemically reacting species (A) and a second species (B) is also present (e.g. oxygen) which also reacts chemically. Viscous heating and Ohmic dissipation are also included to produce a more physically realistic thermal analysis. The non-linear conservation equations proposed here with species diffusion (species A and B) are transformed via an appropriate stream function and scaling variables into a set of non-linear united multi-degree ODEs. The rising nonlinear ordinary differential boundary value problem is solved with four-point Gauss-Lobotto formulae in the MATLAB bvp5c routine. Validation is conducted with an Adams-Moulton predictor-corrector numerical scheme (AM2 coded in Unix). The widespread visualization of velocity, temperature, species A concentration, species B concentration, skin friction, local Nusselt number and species A and B local Sherwood numbers is included.

KEYWORDS: *Darcy-Forchheimer model; aqueous functional magnetic polymer; smart coating flows; Titanium dioxide nanoparticle fraction; non-linear radiation; homogeneous and heterogeneous chemical reactions; numerical; boundary layer enrobing; Nusselt number; Sherwood number*.

1. INTRODUCTION

Modern smart coatings [1] are increasingly being deployed in a wide range of industries to provide enhanced protection under extreme loading environments. These intelligent or functional materials are highly tunable and can be synthesized to any shape or size, with the ability to engineer energy conversions from almost any wavelength to any other wavelength [2]. An important sub-category of these materials are electroactive polymers (EAPs) which combined magnetic particles with polymer melts to create responsive liquids that are easily deposited on engineering components and can be manipulated by external magnetic fields [3]. This permits improved supply chain monitoring and integrity for performance in for example high temperature corrosive environments. Within this group of EAPs there are also temperature-active magnetic hydrogels and magnetic memory polymers which can sense thermal, mechanical, electric, and magnetic stimuli and respond by changing shape, position, stiffness, and other static and dynamical characteristics. These polymers are complex rheologically and comprise colloidal suspensions of particles that form structural chains which can be orientated with respect to the applied magnetic field. Many excellent studies of such functional smart fluids have been communicated in these days. These combine the science of magnetohydrodynamics (MHD) and non-Newtonian fluid dynamics. Weidner [4] investigated the dynamics of ferrofluid coatings within a horizontal cylinder wherein a magnetic field is produced that causes a radially inward force on the dipoles of the ferrofluid. He showed that "over a large range of cylinder radii, the magnetic field can almost completely suppress variations in the coating thickness along the axis of the cylinder caused by surface tension effects leading to improved performance". In recent years with the advent of nanotechnology, electroactive polymers have been produced which feature embedded nanoparticles and nanostructures (tubes, rods) etc. These provide yet further advantages including super-hydrophobic coatings (to mitigate debris deposition) [5], anti-icing properties [6] etc. Many magnetic nanoparticles have been deployed such as Ni–TiN hybrid magneto-nanofluids **[7],** Co-Fe nanocrystals in magnetic polymers [8-10], Ni-Mo [11], chitosan/sodium phytate/nano-Fe_3O_4 for layered magnetic coatings [12] and magnetic Titanium nanostructures [13] which provide enhanced thermal resistance due to the exceptionally high melting point of titanium. In many manufacturing processes for smart nano-coatings, chemical reactions arise. These are used to engineer specific products with customized properties for different applications e.g. coatings for fuel cells, gas turbine blade surfacing, marine vessel hull finishing etc. Many excellent studies of such reactive nano-coating materials processing have been reported including Vorobyev *et al*. [14] who considered chemical reactions in silver nanoparticle thin

film synthesis. Other studies of merit are He *et al.* [15] (who also considered reactive oxygen diffusion), Feng *et al.* [16] (on catalytic reactions in platinum-silver nano hybrid coatings). An excellent appraisal of laboratory methods for chemical reactive nanomaterial synthesis is given by Murr [17]. Further insight into the fabrication of nano-coatings using CNTs (carbon nanotubes) via CVD (chemical vapour deposition) is provided in the review by Kumar and Ando [18]. Commercial procedures are described lucidly by SkySpring Nanomaterials [19], a leading nanocoating company based in Houston, Texas.

To improve on the prediction of the properties and performance of smart magnetic nano-coatings in different applications and furnish a deeper mechanistic appreciation of the actual coating process, mathematical models are indispensable. A popular approach is *nanofluid dynamics*, which emerged from pioneering work conducted at the Argonne Energy Laboratory, Illinois, USA in the mid-1990s directed by Steven Choi. The first book on nanofluids appeared in 2007 [20]. This motivated subsequent developments by establishing certain key mechanisms inherent to nanoscale physics such as Brownian motion, thermophoresis, thermal conductivity enhancement mechanisms, ballistic collisions, micro-convection and other phenomena. Subsequently the methodology reported by Das *et al.* [20] was implemented in many diverse areas of smart coating technology over the past decade or so. These include hydrophobic nanostructured plasma-polymerized intelligent magnetized coatings [21], Nickel-cobalt-silicon carbide electroconductive coatings with enhanced wear properties in manufacturing engineering [22], Nickel-phosphorus and PTFE hybrid magnetic coatings for metallic component surface finishing [23] and titanium-aluminium-vanadium magnetic nanofluid lubricants for surface grinding heat control [24]. Various formulations for simulating nanofluid transport have been developed, notably by Buongiorno [26] at MIT, Koo [27] and Li [28] at North Carolina State University, USA and Tiwari and Das [29] at the Indian Institute of Technology. While all these models provide robust approaches for simulating thermal conductivity enhancement of nanofluids, they differ considerably. Buongiorno's model includes a separate nanoparticle species diffusion equation; it emphasizes the dominance of Brownian diffusion and thermophoresis body force as mechanisms contributing to thermal enhancement. The Koo and Li models are modifications of the Tiwari-Das volume fraction [25] model but only include momentum and energy conservation equations. However, they permit the analysis of nanoparticle type or shape effects which is not possible with the Buongiorno model. As such the Koo-Li and Tiwari-Das models are more realistic for smart magnetic coating flows where different magnetic nanoparticle species can be studied. Buongiorno's model however can compute the distribution of nanoparticle species diffusing in

nanofluids and has been used in several coating simulations of magnetic nano-polymers by Bég *et al.* [29] (using a Williamson viscoelastic model and considering wall thermal slip) and Shukla *et al.* [30] (who considered second law thermodynamic optimization of magnetic nano-coatings).

In many fabrication techniques, high temperature conditions are present. In addition to conduction and convection modes, thermal radiation is also invoked [31, 32]. The most complex of heat transfer modes, radiation is challenging due to the *integro-differential* nature of the governing equation. "Thermal conductivity and radiative absorption of magnetic aqueous nanofluids (nano-polymers) increase with temperature while they tend to reduce in non-aqueous nanofluids. Thermal radiative heat transfer is therefore important in the synthesis of magnetic nano-polymers". When conduction and convection are also present, nonlinearity renders the transport equations in coating flows very challenging to solve, even with state-of-the-art software. Rather than deploying advanced Monte Carlo solvers, to solve the full system of equations, algebraic flux models, originally developed for astrophysics, are often implemented. These augment the energy conservation equation with extra radiative flux terms. The Rosseland diffusion flux model is most popular in boundary layer models of coating flows and is generally valid for low optical thickness fluent gray media which can absorb and emit but not scatter thermal radiation. It allows radiative heat transfer to be simulated as a differential flux term rather than with integrals. Rajesh *et al.* [33] studied the time-dependent oscillatory nanofluid coating boundary layer flow on a vertical pipe with strong radiative flux using a finite difference method. They considered four types of metallic nanoparticle i.e. Al_2O_3, Cu, TiO_2 and Ag studied flows with nanoparticle volume fractions up to 4% doping. They presented extensive results for skin friction and wall Nusselt number observing a substantial elevation also in temperatures with greater radiative flux contribution.

In the above studies of coating flows external to different configurations, the substrate was assumed to remain of constant length. However, high temperature nano-coating systems often feature stretching of the substrate to produce a more uniform coating distribution. Stretching may be linear, quadratic, exponential or of other forms. Magnetic nanocoating flows on stretching (or contracting) horizontal surfaces have been examined by several authors in recent years. Uddin *et al.* [34] used Maple quadrature routines to compute the heat, mass and momentum characteristics in incompressible extending/shrinking plate substrate boundary layer magnetic nanofluid flow doped with gyrotactic micro-organisms ("nano-bioconvection"). Ferdows *et al.* [35] used an explicit finite difference technique to simulate the effect of uni-directional radiative flux on unsteady nanofluid flow from a porous stretching substrate. Both

these studies employed the Buongiorno nanoscale model. In many coating applications, cylindrical geometries arise. Cylinders are fundamental to pipeline, aerospace, energy and nuclear engineering where high temperatures can induce significant surficial degradation and corrosion. Coating flows of cylinders therefore constitute a very important area of transport phenomena. Studies in this area have addressed multiple phenomena including coating thickness, surface tension, interfacial instability, gravity effects and van der Waals forces. An advantage of cylindrical coating flows is that quasi- 3-dimensional models can be developed since the regime is axisymmetric (i.e. reduction of 3 space variables to 2 space variables). However, cylinder curvature may or may not exert a significant role in such flows. Preziosi and Joseph [36] examined experimentally the coating of a Newtonian liquid on a revolving cylinder. They showed that free surface variation along the axial direction on the coating layer are controlled by interplay between capillarity and centripetal acceleration similar to that which determines the shape of rotating drops and bubbles in the absence of gravity. They also showed that the coating can be sustained on the horizontal rotating cylinder provided viscous forces pulling the liquid around with the cylinder are large enough to overcome the force of gravity. However, they also observed that at locations on the cylinder where the thickness of the layer exceeds a critical value, the excess fluid will run off. Prasad *et al.* [37] generalized the study in [36] to consider heat transfer in viscoplastic coating flow on a porous horizontal cylinder with hydrodynamic and thermal wall slip effects and wall suction/injection. They deployed a second order accurate finite-difference scheme. They observed that greater momentum slip accelerates the boundary layer coating the flow near the cylinder surface but induces deceleration further towards the free stream. They also observed that the thermal boundary layer thickness is weakly reduced for stronger viscoplastic characteristics and that strong blowing (injection) at the cylinder surface accelerates the flow. Weidner *et al.* [38] deployed an alternating-direction implicit algorithm and lubrication theory to compute the thin coating flow dynamics on a horizontal right circular cylinder. They identified that the initial gravity-dominated drainage from the top and sides of the cylinder inhibits the formation of any axial disturbances, although when this effect weakens, longitudinal waves emerge at the base of the bottom of the cylinder. They also noted that more accurate results of the evolving coating profile are obtained with viscous dissipation included. Prasad *et al.* [39] computed the heat and momentum characteristics in incompressible axisymmetric polymeric flow over a horizontal isothermal circular cylinder using the Jeffreys elastic-viscous model. They observed that the momentum boundary layer thickness is increased (flow is retarded) with greater Deborah number (ratio of the characteristic time of relaxation to the characteristic time of experiment or observation)

and similarly the thermal boundary layer thickness is also enhanced. They also noted that higher Debroah number suppresses wall Nusselt number (heat transfer rate) whereas greater ratio of relaxation to retardation times elevates it. Weidner [40] investigated computationally the dynamics of plummet structure in ferrous magnetic fluid coating. He considered the transition from a uniform coating to the generation of undulations and eventual final configuration of distinct drop, noting that magnetic (Lorentz) forces generally oppose gravity effects and reduce the drainage rate at the cylinder base. He also demonstrated that the final coating is not restricted to the cylinder base and enrobes the entire circumference of cylinder when magnetic field is adequately strong. More recently Reddy *et al.* [41] studied the transient flow deposition of a micropolar magnetic polymer coating on a vertical cylinder with strong radiation heat flux using an optimized Crank-Nicolson finite difference method. They showed that with stronger Hartmann number (ratio of magnetic body force to viscous force), or radiative flux, a greater time elapse is required to attain the *time-independent state* increases. Using Bejan's heat flow visualization technique, they also find "stronger radiation or magnetic parameter values result in an increase in the deviation of heat lines from the hot wall". They further observed that the magnetic polymer heat lines depart weakly from the hot cylinder wall with greater values of Eringen micropolar vortex viscosity parameter (rheological parameter). These studies were confined to constant length cylinders. Coating flows on s*tretching cylinders* have however more recently received some attention in the scientific literature. Bilal *et al.* [42] examined the catalytic reaction effects in magnetic viscoelastic polymer flow on a stretching cylinder with thermal conductivity variation thermal relaxation effects (non-Fourier conduction) and the Williamson rheological model. They used Mathematica shooting solvers to show that with greater thermal stratification and curvature parameter values, flow is accelerated, and the regime is heated. They also observed that stronger thermal relaxation increases wall skin friction on the cylinder surface and stretching induces a delay in boundary layer growth. Pandey and Kumar [43] presented numerical solutions for copper-water nanofluid flow from an extending cylinder with heat generation/absorption and radiative effects. They observed that with decreasing radiative flux thermal boundary layer thickness is reduced whereas skin friction is enhanced with increasing thermal radiation and heat source. Zaib *et al.* [44] computed the impact of thermal radiation on mixed convective enrobing flow of a copper–water nanofluid along a porous shrinking cylinder with homogeneous–heterogeneous reactions with a Tiwari-Das type model. They examined both buoyancy-assisted and opposed flow identifying dual solutions for the opposing flow (with a particular value of wall suction) and a unique single solution for the assisting flow. Increasing nanoparticle

fraction and mixed convective parameter were also observed to delay boundary layer separation. Mahdy [45] conducted a second law thermodynamic analysis of steady hydromagnetic nanofluid coating flow on an accelerating cylinder with erratic wall temperature. He considered Cu, Ag, Al_2O_3, and TiO_2 nanoparticles with a water base fluid. He showed using a finite difference solution of the dimensionless transformed conservation equations that temperature is suppressed with mixed convection parameter whereas it is boosted with greater nanoparticle volume fraction, curvature and magnetic parameters. He also noted that entropy generation is elevated with greater curvature of the cylinder, Reynolds number, and mixed convection parameters, whereas it is depressed with stronger radial magnetic field. Shamshuddin *et al*. [46] used a spectral computational algorithm to simulate the axisymmetric boundary layer coating flow of a ferrohydrodynamic nanofluid on a stretching cylinder with magnetic induction effects at high magnetic Reynolds number. They studied aqueous ferro-polymers with magnetic (Manganese Franklinite (MnZnFe2O4), Ferric Oxide (Fe3O4)) and also compared performance with non-magnetic (Silicon Dioxide (SiO2), Nimonic 80a) nanoparticles. Their computations indicated that greater values of magnetic Prandtl number induce flow retardation whereas they mobilize intensified heating (thicker thermal boundary layers). Maximum coating flow acceleration was achieved with non-magnetic nanoparticles (SiO2) further augmentation in temperature was produced with magnetic nanoparticles (Fe3O4). They further showed that flow is accelerated, temperatures boosted, and greater magnetic induction generated with larger cylinder curvature parameters. Hashim *et al*. [47] employed a fifth-order Runge-Kutta Fehlberg integration scheme to simulate the enrobing phase-change boundary layer flow of non-Newtonian Carreau fluid over a linearly stretching cylinder, observing that intensified melting accelerates the flow and stretching also contributes to greater flow velocity compared with a constant length cylinder. Nusselt number is however suppressed with greater melting and Weissenberg viscoelastic numbers.

In the present work we consider the *forced convection coating boundary layer flow of a magnetic polymeric nanofluid on a stretching cylinder in a porous medium under radial magnetic field. Radiative heat flux, heat generation, non-Darcy effects and dual reactive species are also considered which constitute the novelty of the present investigation*. Porous media have been deployed industrially to achieve better conformation of coatings [48, 49]. High permeability media engulfing coating flows have also found some promise in the controlled deposition of smart intumescent coatings for fire protection [50]. From the macroscale, simpler governing equations such as Darcy's law and the Kozeny-Carman

equation, have provided popular in porous media materials processing simulations. Darcy's law is an empirical law which states that in steady flow through porous media, the flow rate is proportional to the applied pressure gradient. For the case of isotropic porous media a single permeability in all directions is used. Darcy's law is valid for a densely packed porous medium with very low permeability and takes into account only the frictional force offered by the solid particles to the fluid rather than the usual viscous shear. However notable studies in porous media hydrodynamics have shown that at higher Reynolds numbers (within the laminar regime), second order inertial drag effects arise [51]. When the porosity of the porous medium is close to unity, the flow of fluid is curvilinear, and curvature of the path gives rise to the inertia effect. As the inertia force increases relative to the viscous force, the streamlines become more distorted and drag increases more rapidly with velocity. Even at higher Reynolds number there is a transition in the flow, but not from laminar to turbulent. A change from linear drag (Darcy model) to non-linear drag is observed [52]. Engineers have therefore developed a Darcy-Forchheimer second order drag force model which simulates porous media impedance both at low Reynolds numbers (Darcy term) and inertial drag at higher Reynolds numbers (Forchheimer second order term) [53, 54]. Unsteadiness effects can also become significant in the Forchheimer regime although the primary effect is a sharp elevation in matrix fiber resistance [55]. The Darcy-Forchheimer model has been successfully implemented in a number of coating flow studies for cylindrical bodies. For example, Zueco *et al.* [56] used a network electrothermal simulation code, PSPICE, to analyze the double-diffusive axisymmetric boundary layer flow from a cylinder with first order homogenous chemical reaction effects in a Darcy-Forchhemer porous medium. In the current analysis, *linear stretching* of the cylinder is considered [57-60] i.e. the cylinder is extended axially with a constant linear velocity. Titanium dioxide nanoparticles are studied and the nanoscale behaviour is analyzed with a Tiwari-Das volume fraction formulation which has also been employed recently to analyze smart magnetic solar collector coatings [61] and is simpler than the KKL nanoscale model [62]. Furthermore, unlike the Buongiorno model [63] the Tiwari-Das model allows actual nanoparticle material types to be studied. Viscous heating and Ohmic dissipation are included in the present study and a heat source (e.g. laser-generated surficial finishing [64- 66] is featured to produce more physically realistic thermal distribution predictions in coating flows. The non-linear conservation equations for mass, momentum, energy and species diffusion (species A and B) are transformed via an appropriate stream function and scaling variables into a system of non-linear coupled multi-degree ordinary differential equations (ODEs). The emerging nonlinear ordinary differential boundary value problem is solved with four-point

Gauss-Lobotto formulae in the MATLAB bvp5c routine [67, 68]. Validation is conducted with an Adams-Moulton predictor-corrector numerical scheme [69]. Extensive visualization of velocity, temperature, species A concentration, species B concentration, skin friction, local Nusselt number and species A and B local Sherwood numbers is included. Detailed physical interpretation is presented, and some pathways are also recommended for generalization of the current model in the future. The study is relevant to high temperature enrobing smart magnetic nanocoating manufacturing fluid dynamics of cylindrical engineering components. The current study constitutes an original contribution in smart coating nanofluid dynamics and has to the authors' knowledge not been communicated thus far in the engineering science literature.

2. ELECTROCONDUCTIVE NANOPOLYMER COATING FLOW MODEL

Steady axisymmetric magnetohydrodynamic (MHD) flow of an electro-conductive viscous incompressible nanofluid, from a horizontal stretching cylinder of radius a, and initial unstretched length l, adjacent to a homogenous, isotropic porous medium is studied as a model of magnetic nano-coating enrobing processes.
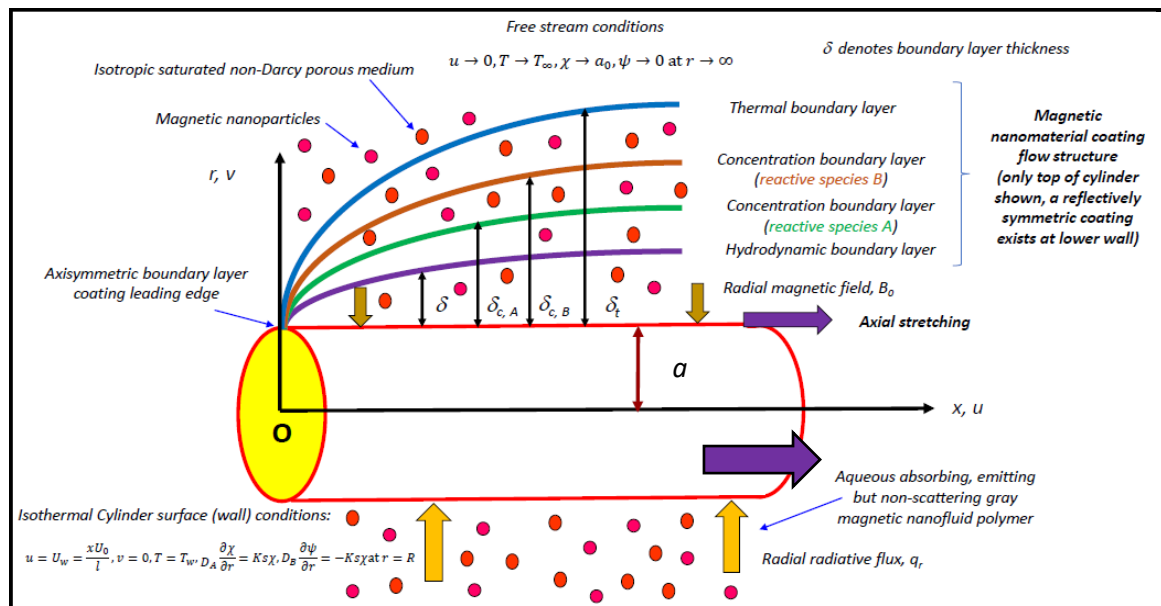

Fig. 1 Axisymmetric coating flow of magnetic nanofluid on a horizontal stretching cylinder

Heat source, viscous and Ohmic dissipation (Joule heating) are present. Two species (A, B) of a reactive nature are present and both homogeneous and heterogeneous cases in catalytic surface reactions are studied. A uniform static magnetic field is imposed in the radial direction. A cylindrical coordinate system is adopted with 'x' and 'r' along the axial and normal directions (**Fig.1**). Magnetic field is of insufficient strength to mobilize induction effects and the surface of the cylinder is electrically non-conducting and thermally insulated. The cylinder

is stretched along the *x*-axis keeping the origin fixed at a constant velocity, U_w ("linear stretching"). The Tiwari-Das nanoscale model [25] is deployed, assuming a dilute nanofluid and local thermal equilibrium between the nanoparticles and the fluid-saturated porous medium. However *mass diffusion of the nanoparticles* is not simulated. Electrical field effects are ignored. The dual species present generate separate concentration boundary layers. The TiO_2 nanoparticles are one chemically reacting species (A) and a second species (B) is also present (e.g. oxygen) which also reacts chemically. These species produce homogeneous and heterogeneous catalytic reactions at the surface of the cylinder, which are modelled following [60] with the following relation:

$$A + 2B \rightarrow 3B, rate = K\chi\psi^2 \tag{1}$$

The single, isothermal and first order reaction on the catalyst is represented by:

$$A + B \rightarrow 3B, \ rate = Ks\chi \tag{2}$$

Here χ and ψ are the concentrations of the chemical species A and B, K and Ks are the respective homogenous and heterogenous reaction rate constants. The Rosseland diffusion algebraic approximation for radiative heat transfer is utilized and optical thickness of the magnetic nanofluid coating assumed to be large. The gray approximation is employed for which radiation is absorbed or emitted at the cylinder boundary but not scattered. Intrinsic to this model is the assumption that the intensity is the *black-body intensity* at the fluid temperature. It is valid generally for incompressible flows as considered here. Radial radiative flux is approximated using the Rosseland model - see Bég *et al.* [70]. Extending the formulation in Qayyum *et al.* [71] to incorporate *viscous heating. Joule heating (Ohmic dissipation), second order inertial (Forchheimer) drag and heat source effect*, the resulting conservation equations emerge in a cylindrical (*r, x, z*) coordinate system as:

$$\frac{\partial u}{\partial x} + \frac{v}{r} + \frac{\partial v}{\partial r} = 0 \tag{3}$$

$$\rho_{nf}\left(u\frac{\partial u}{\partial x} + v\frac{\partial u}{\partial r}\right) = \mu_{nf}\left(\frac{\partial^2 u}{\partial r^2} + \frac{1}{r}\frac{\partial u}{\partial r}\right) - \left(\sigma_{nf}B_0 + \frac{\mu_{nf}}{K^*}\right)u - \rho_{nf}\frac{I^*}{\sqrt{K^*}}u^2 \tag{4}$$

$$(\rho c_p)_{nf}\left(u\frac{\partial T}{\partial x} + v\frac{\partial T}{\partial r}\right) = k_{nf}\frac{1}{r}\frac{\partial}{\partial r}\left(r\frac{\partial T}{\partial r}\right) - \frac{1}{r}\frac{\partial}{\partial r}(rq_r) + \sigma_{nf}B_0^2 u^2 + Q_0(T - T_\infty) \tag{5}$$

$$u\frac{\partial \chi}{\partial x} + v\frac{\partial \chi}{\partial r} = D_A\left(\frac{\partial^2 \chi}{\partial r^2} + \frac{1}{r}\frac{\partial \chi}{\partial r}\right) - k_1\chi\psi^2 \tag{6}$$

$$u\frac{\partial \psi}{\partial x} + v\frac{\partial \psi}{\partial r} = D_B\left(\frac{\partial^2 \psi}{\partial r^2} + \frac{1}{r}\frac{\partial \psi}{\partial r}\right) + k_1\chi\psi^2 \tag{7}$$

$$\left.\begin{array}{l} u = U_w = \frac{xU_0}{l}, v = 0, T = T_w, D_A\frac{\partial \chi}{\partial r} = Ks\chi, D_B\frac{\partial \psi}{\partial r} = -Ks\chi \text{ at } r = a \\ u \to 0, T \to T_\infty, \chi \to a_0, \psi \to 0 \text{ at } r \to \infty \end{array}\right\} \tag{8}$$

Here the following expressions define the material property ratios:

$$\mu_{nf} = \frac{\mu_f}{(1-\phi)^{2.5}}, \rho_{nf} = (1-\phi)\rho_f + \phi\rho_s, (\rho c_p)_{nf} = (1-\phi)(\rho c_p)_f + \phi(\rho c_p)_s,$$

$$\sigma_{nf} = \sigma_f\left[1 + \frac{3(\Omega-1)\phi}{(\Omega+2)-\phi(\Omega-1)}\right], \Omega = \frac{\sigma_s}{\sigma_f}, k_{nf} = k_f\left[\frac{k_s+2k_f-2\phi(k_f-k_s)}{k_s+2k_f+\phi(k_f-k_s)}\right] \tag{9}$$

The uni-directional radiative heat flux is imposed in the radial direction around the cylinder longitudinal surface and takes the form:

$$q_r = \frac{4\sigma^*}{3k^*}\frac{\partial T^4}{\partial r} = -\frac{16\sigma^*}{3k^*}T^3\frac{\partial T}{\partial r} \tag{10}$$

Here σ^* is the Stefan-Boltzmann constant and k^* is the mean absorption coefficient. To non-dimensionalize the conservation equations and associated boundary conditions (3)-(8), the following transformation variables are invoked [71]:

$$\eta = \frac{r^2-a^2}{2a}\sqrt{\frac{u_0}{lv_f}}, u = \frac{xu_0}{l}f'(\eta), v = -\frac{a}{r}\sqrt{\frac{v_f u_0}{l}}f(\eta), \theta(\eta) = \frac{T-T_\infty}{T_w-T_\infty}, g(\eta) = \frac{\chi}{a_0}, h(\eta) = \frac{\psi}{a_0}. \tag{11}$$

The incompressibility condition (continuity equation) is automatically satisfied and the boundary layer Eqns. (3) - (7) emerge as:

$$A_2\left((1+2\gamma\eta)f''' + 2\gamma f''\right) - \left(MA_3 + A_2 K_p^{-1}\right)f' + A_1\left(ff'' - \left(1+I_f\right)f'^2\right) = 0 \tag{12}$$

$$\frac{1}{Pr}\left(A_4 + Nr\left(1+(\theta_w-1)\theta\right)^3\right)\left((1+2\gamma\eta)\theta'' + 2\gamma\theta'\right) + A_3 MEc\left(f'\right)^2$$

$$+3Nr\left(1+(\theta_w-1)\theta\right)^2(\theta_w-1)(1+2\gamma\eta)\left(\theta'\right)^2 + A_5 f\theta' + S\theta = 0 \tag{13}$$

$$\frac{1}{Sc}\left((1+2\gamma\eta)g'' + 2\gamma g'\right) + fg' - Kgh^2 = 0 \tag{14}$$

$$\frac{1}{Sc}\left((1+2\gamma\eta)h'' + 2\gamma h'\right) + fh' + Kgh^2 = 0 \tag{15}$$

$$\begin{array}{l} f = 0, f' = 1, \theta = 1, g' = K_s g, \delta h' = -K_s g \text{ at } \eta = 0, \\ f' \to 0, \theta \to 0, g \to 1, h \to 1 \text{ as } \eta \to \infty. \end{array} \tag{16}$$

The dimensionless numbers featured are defined as follows:

$$\gamma = \sqrt{\frac{lv_f}{u_0 a^2}}, M = \frac{\sigma_f a B_0^2}{\rho_f u_0}, Kp = \frac{u_0 K_p^*}{v_f a l}, I_f = \frac{xal^*}{\mu_f \sqrt{K^*}}, Pr = \frac{u_0 v_f}{k_f}, \theta_w = \frac{T_w}{T_\infty}, Nr = \frac{16\sigma^* T_\infty^3}{3k^* k_f}, \left.\begin{array}{c} \\ \\ \end{array}\right\}$$
$$Ec = \frac{u_0 x^2}{(\rho c_p)_f T_\infty(\theta_w - 1)}, S = \frac{Q_0}{u_0 l}, Sc = \frac{\alpha_f}{D_A}, \delta = \frac{D_B}{D_A}, K = \frac{a_0^2 l k_1}{u_w}, K_s = \frac{k_s^*}{D_A}\sqrt{\frac{v_f l}{u_0}}. \tag{17}$$

Furthermore, the dimensionless material property ratios emerging are:

$$A_1 = \frac{\rho_{nf}}{\rho_f}, A_2 = \frac{\mu_{nf}}{\mu_f}, A_3 = \frac{\sigma_{nf}}{\sigma_f}, A_4 = \frac{k_{nf}}{k_f}, A_5 = \frac{(\rho c_p)_{nf}}{(\rho c_p)_f}. \tag{18}$$

It is important to note that when $r = a$, this corresponds to the *surface of the cylinder* for which $\eta = 0$. In the special case of *equivalent mass diffusivities of both species*, $D_A = D_B$ and $\delta = 1$ and it follows that:

$$g(\eta) + h(\eta) = 1 \tag{19}$$

Eqns. (14) and (15) for this scenario may be replaced by:

$$\frac{1}{Sc}\left((1 + 2\gamma\eta)g'' + 2\gamma g'\right) + fg' - Kg(1 - g)^2 = 0 \tag{20}$$

The assimilated modified boundary condition can be contracted to:

$$f = 0, f' = 1, \theta = 1, g' = K_s g \text{ at } \eta = 0,$$
$$f' \to 0, \theta \to 0, g \to 1, h \to 1 \text{ as } \eta \to \infty. \tag{21}$$

This permits a single Schmidt number to be deployed in the analysis for both species A and B, although the species concentrations g, h are not quantitively the same due to the difference in the polarity of the homogeneous/heterogeneous catalytic reaction terms i.e. the last terms on the left hand side of Eqns. (14) and (15) – in the case of species A the term is negative i.e. destructive, whereas in the case of species B it is positive i.e. constructive. The dimensional wall skin friction C_{fx} and local Nusselt number (wall heat transfer rate) Nu_x are defined as:

$$C_{fx} = \frac{\tau_w}{\rho_f u_w^2}, Nu_x = \frac{xq_w}{k_f(T_w - T_\infty)} \tag{22}$$

Here τ_w, shear stress, and q_w, surface heat flux are defined by:

$$\tau_w = \mu_{nf}\left(\frac{\partial u}{\partial r}\right)_{r=a} \tag{23}$$

$$q_w = \left(-k_{nf}\frac{\partial T}{\partial r} + \frac{\partial q_r}{\partial r}\right)_{r=a} \tag{24}$$

These lead to the following expressions for the *dimensionless skin friction* and *local Nusselt number*:

$$C_{fx} = C_f Re_x^{0.5} = A_2 f''(0) \tag{25}$$

$$Nu_x = Nu Re_x^{-0.5} = -[A_4 + Nr(1 + (\theta_w - 1)\theta(0))^3]\theta'(0) \tag{26}$$

The surface mass flux for each species A and B is defined as:

$$q_{m\,(A)} = -D_A \left(\frac{\partial \chi}{\partial r}\right)_{r=a} \tag{27}$$

$$q_{m\,(B)} = -D_B \left(\frac{\partial \psi}{\partial r}\right)_{r=a} \tag{28}$$

The local Sherwood numbers for species A and B i.e. dimensionless mass transfer rates at the cylinder surface are defined using the mass fluxes as:

$$Sh_{x\,(A)} = \frac{x q_{m(A)}}{D_A(\chi_w - \chi_\infty)} \tag{29}$$

$$Sh_{x\,(B)} = \frac{x q_{m(B)}}{D_B(\psi_w - \psi_\infty)} \tag{30}$$

In terms of the transformed dimensional concentration functions for species A and B i.e. *g (η) and h (η)* we have:

$$Sh_{x,A} = -g'(0) \tag{31}$$

$$Sh_{x,B} = -h'(0). \tag{32}$$

In the above definitions, Re_x is the local Reynolds number and given by $Re_x = \frac{u_0 x}{v_f}$. It is also noteworthy that Qayyum *et al.* [71] do not consider Sherwood number behaviour in their study and the present article therefore generalizes their analysis. All parameters and units are defined in the notation section at the end of the article.

3. NUMERICAL SOLUTIONS WITH MATLAB BVP5C SOLVER

The transformed nonlinear ODE boundary value problem for the *triple diffusive coating flow* defined by Eqns. (12)-(15) under wall and free stream boundary conditions (16) is a 9th order, coupled, multi-degree system. This requires a numerical solution due to the strong nonlinearity. In this regard the MATLAB bvp5c solver is deployed. This is a superior algorithm to the more customary bvp4c solver, and directly controls the true error in the calculation, while bvp4c controls it only indirectly. At more stringent error tolerances, this difference between the solvers is not as apparent as noted by Shampine and Kierzenka [68]. The "bvp5c is a finite difference code that implements the four-stage Lobatto IIIa formula which is a collocation formula and the collocation polynomial provides a C^1-continuous solution that is fifth-order accurate uniformly in [a,b]. The formula is implemented as an implicit Runge-Kutta formula". The bvp5c does not utilize analytical condensation which is present in bvp4c. Unlike bvp4c which handles unknown parameters directly, bvp5c augments the system with trivial differential equations for the unknown parameters. For robustness the new solver is based on

control of a residual. The residual is scaled so that it has the same order of convergence as the true error. For a large class of methods, bvp5c [68] has been verified to confirm that if this scaled residual is less than a given tolerance, then asymptotically the true error is also less than the tolerance. The bvp5c interpolates the value and gradient at both ends of the subinterval and the value of Y_{MID} at the midpoint. The following stepping formula is used as elaborated by Russel and Christansen [72]:

$$Y_{MID} = Y_1 + \zeta \left[\frac{17}{192} K_1 + \frac{40 + 15\sqrt{5}}{192} K_2 + \frac{40 - 15\sqrt{5}}{192} K_3 - \frac{1}{192} K_4 \right] \tag{33}$$

Here Y_1 is the initial guess and K_1, K_2, K_3, K_4 are the approximations with a stepping distance of ζ. The algorithm is very efficient, unconditionally stable and produces excellent accuracy with fast compilation times.

4. VALIDATION WITH ADAMS–MOULTON TWO-STEP PREDICTOR CORRECTOR SCHEME

Since the present model is novel, there are no solutions against which to benchmark the BVP5C finite difference results. Although an attempt has been made to validate with the earlier study of Qayyum *et al.* [71], unfortunately insufficient data is given in the Tables in that article. Also, the solutions in [71] have considered *copper-water and silver-water nano-coatings*, which are not considered in our study. To validate the computations for *titanium oxide aqueous nano-polymers*, therefore, an alternate numerical method is therefore deployed, namely the Adams Moulton predictor-corrector method [69]. This verification approach also has the significant advantage that the full model developed in the current work can be validated i.e. with Non-Darcy, heat source, viscous heating and Ohmic dissipation effects, all of which are absent in the earlier study of Qayyum *et al.* [71]. The Adams Moulton method is an implicit multistep method. A popular version is the rapidly convergent, stable 2-step Adams Moulton method for a linear initial value problem. Applying this algorithm to the present boundary value problem, we define the gradients of the *dimensionless stream function (f), temperature (θ), species A concentration (g) and species B concentration (h)* as follows using a general function, *v*:

$$\frac{df}{d\eta} = v(\eta, f), f(\eta_0) = f_0 \tag{34}$$

$$\frac{d\theta}{d\eta} = v(\eta, \theta), \theta(\eta_0) = \theta_0 \tag{35}$$

$$\frac{dg}{d\eta} = v(\eta, \theta), g(\eta_0) = g_0 \tag{36}$$

$$\frac{dh}{d\eta} = v(\eta, \theta), h(\eta_0) = h_0 \tag{37}$$

Heref_0, θ_0, g_0, h_0 are initial guesses. The *predictors* are then specified and thereafter the correctors to produce an accurate solution based on the initial calculation. The Adams-Moulton two-step *predictor relations* for the four variables, with a stepping distance of ζ, take the form:

$$f_{k+1} = f_k + \frac{\zeta}{2}\big(3v(\eta_k, f_k) - v(\eta_{k-1}, f_{k-1})\big) \tag{38}$$

$$\theta_{k+1} = \theta_k + \frac{\zeta}{2}\big(3v(\eta_k, \theta_k) - v(\eta_{k-1}, \theta_{k-1})\big) \tag{39}$$

$$g_{k+1} = g_k + \frac{\zeta}{2}\big(3v(\eta_k, g_k) - v(\eta_{k-1}, g_{k-1})\big) \tag{40}$$

$$h_{k+1} = h_k + \frac{\zeta}{2}\big(3v(\eta_k, h_k) - v(\eta_{k-1}, \varphi_{k-1})\big) \tag{41}$$

The corresponding two-step *corrector* formulae are given by:

$$f_{k+1} = f_k + \frac{\zeta}{2}\big(v(\eta_{k+1}, f_{k+1}) - v(\eta_k, f_k)\big) \tag{42}$$

$$\theta_{k+1} = \theta_k + \frac{\zeta}{2}\big(v(\eta_{k+1}, \theta_{k+1}) - v(\eta_k, \theta_k)\big) \tag{43}$$

$$g_{k+1} = g_k + \frac{\zeta}{2}\big(v(\eta_{k+1}, g_{k+1}) - v(\eta_k, g_k)\big) \tag{44}$$

$$h_{k+1} = h_k + \frac{\zeta}{2}\big(v(\eta_{k+1}, h_{k+1}) - v(\eta_k, h_k)\big) \tag{45}$$

The second order Adams-Moulton (AM2) is an implicit technique and sometimes referred to as the *trapezoidal* rule. The implicit nature of the method is evident. For a non-linear boundary value problem, *non-linear algebraic equations* are solved at each step iteratively. This is much more expensive as compared to the explicit AB2 method. However, being an implicit technique, AM2 does not suffer from the numerical instability of the AB2 for relatively large values of the stepping distance. As with all numerical methods, there is an intrinsic trade-off between stability and computational cost, since both AM2 and AB2 are second order accurate. To verify the Matlab bvp4c solutions, the following data for Titanium dioxide-aqueous nano-polymer coating is prescribed (Table 2). In the benchmarking, the following data is prescribed: $\gamma = 0.01, M = 1, Kp = 0.5, I_f = 1, Pr = 2, \theta_w = 1.5, Nr = 0.1, Ec = 0.5, S = 0.01, K = 2, K_s = 0.01, Sc = 0.22$. This data corresponds to practical aqueous metallic nano-polymers. The Prandtl number of water is usually 7, and that of metallic nanoparticles much lower liquid metal Prandtl numbers are of the order of 0.01); combining these two materials yields Prandtl numbers *greater than unity but much less than pure water* i.e. *Pr = 2* [73]. The Schmidt number prescribed (*Sc = 0.22*) corresponds to oxygen and hydrogen diffusing in aqueous polymers as noted by Incropera *et al.* [74] for which the mass diffusion rate of species A (oxygen) and

species B (hydrogen) greatly exceeds the viscous diffusion rate (Schmidt number is the ratio of viscous diffusivity and mass (species) diffusivity).

Table 1: Mechanical, thermal and electrical properties of base fluid and metallic nanoparticles

Property	ρ_f	$(c_p)_f$	k_f	$(\beta_T)_f$	σ_f
Aqueous polymer (water)	997.1(kg/m^3)	4179 J/kgK	0.613W/mK	$21 * 10^{-6}$/K	0.5 Siemens/m
Property	ρ_s	$(c_p)_s$	k_s	$(\beta_T)_s$	σ_s
Titanium dioxide nanoparticles	4250 kg/m^3	686.2 J/kgK	8.9538 W/mK	$0.90 * 10^5$/K	$2.5 * 10^6$Siemens/m

In **Fig. 2 a-d**, we have plotted the comparisons for cylinder surface skin friction versus nanoparticle volume fraction and also temperature, species A concentration (oxygen) and species B (hydrogen) versus transverse coordinate which have been obtained with MATLAB bvp5c and the AM2 code programmed in Unix on an SGI Octane desktop workstation, for which compilation times typically take seconds on this machine. (Default data as in **Table 1**).
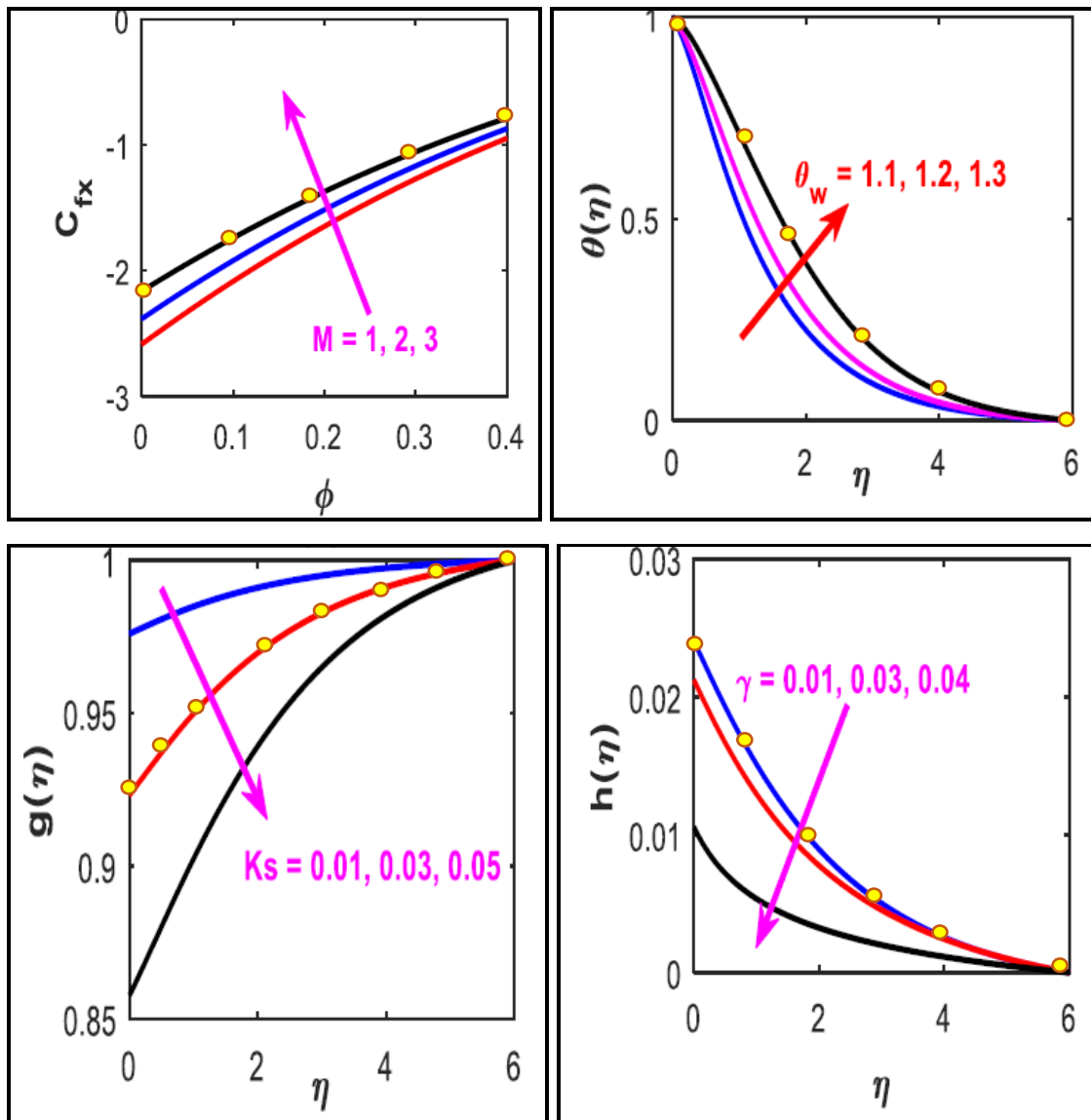
Fig. 2 (a) Skin friction, **(b)** temperature, **(c)** species A concentration and **(d)** species B concentration evolution. MATLAB bvp5c – solid lines, AM2 – yellow dots (o).

Excellent correlation is achieved. Confidence in the MATLAB bvp5c solution is therefore justifiably very high. Full visualization of computations is presented in section 5.

5. MATLAB RESULTS AND DISCUSSION

Figs. 3- 21 illustrate the MATLAB results for velocity, temperature, species A concentration, species B concentration, skin friction, local Nusselt number, species A local Sherwood number and species B local Sherwood number.
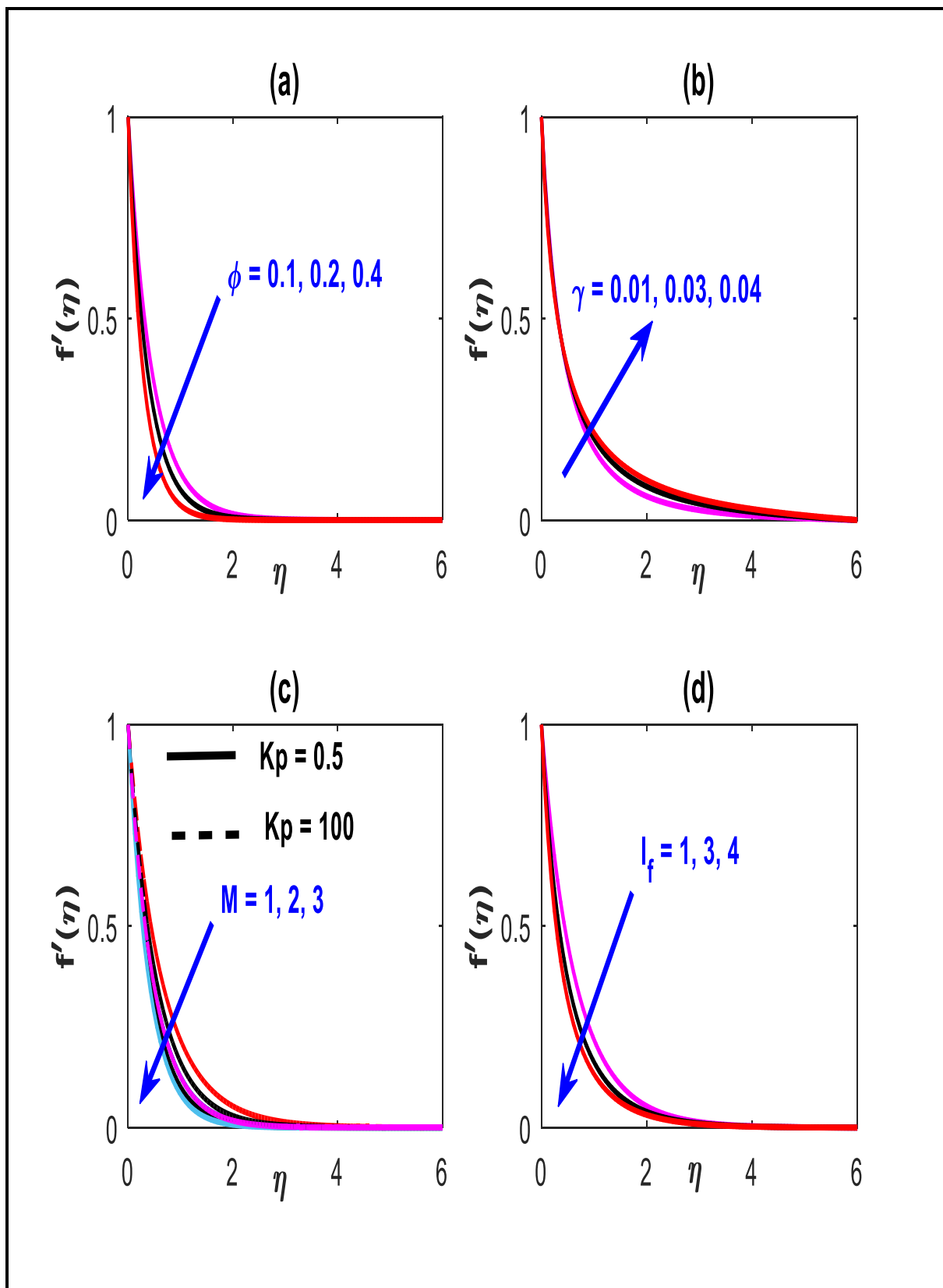
Fig. 3 Evolution of velocity with transverse coordinate for (a) nanoparticle volume fraction (b) curvature parameter (c) magnetic Stuart number and Darcian parameter (d) Forchheimer inertial porous media parameter.
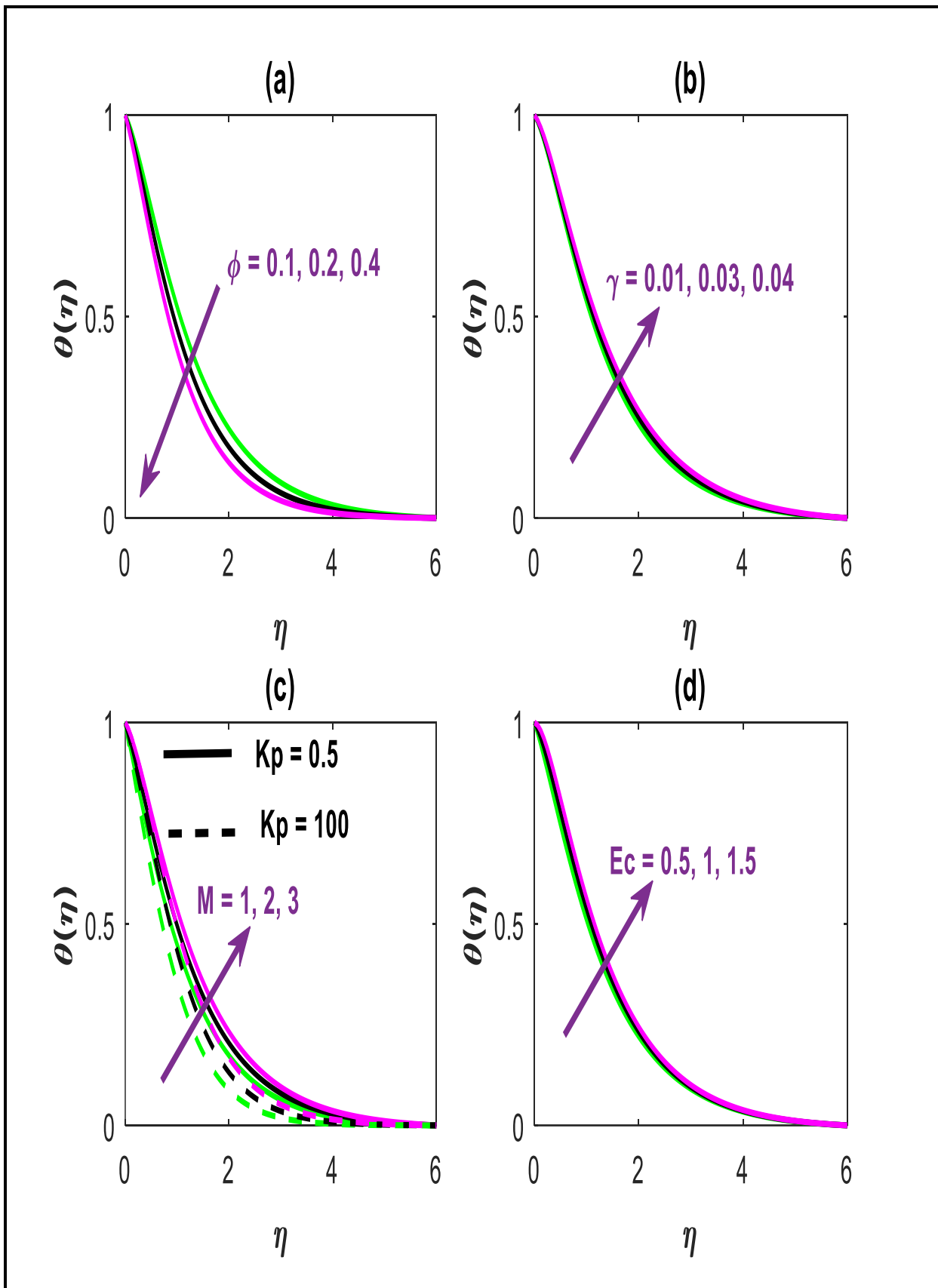
Fig. 4 Evolution of temperature with transverse coordinate for (a) nanoparticle volume fraction (b) curvature parameter (c) magnetic Stuart number and Darcian parameter (d) Eckert number.
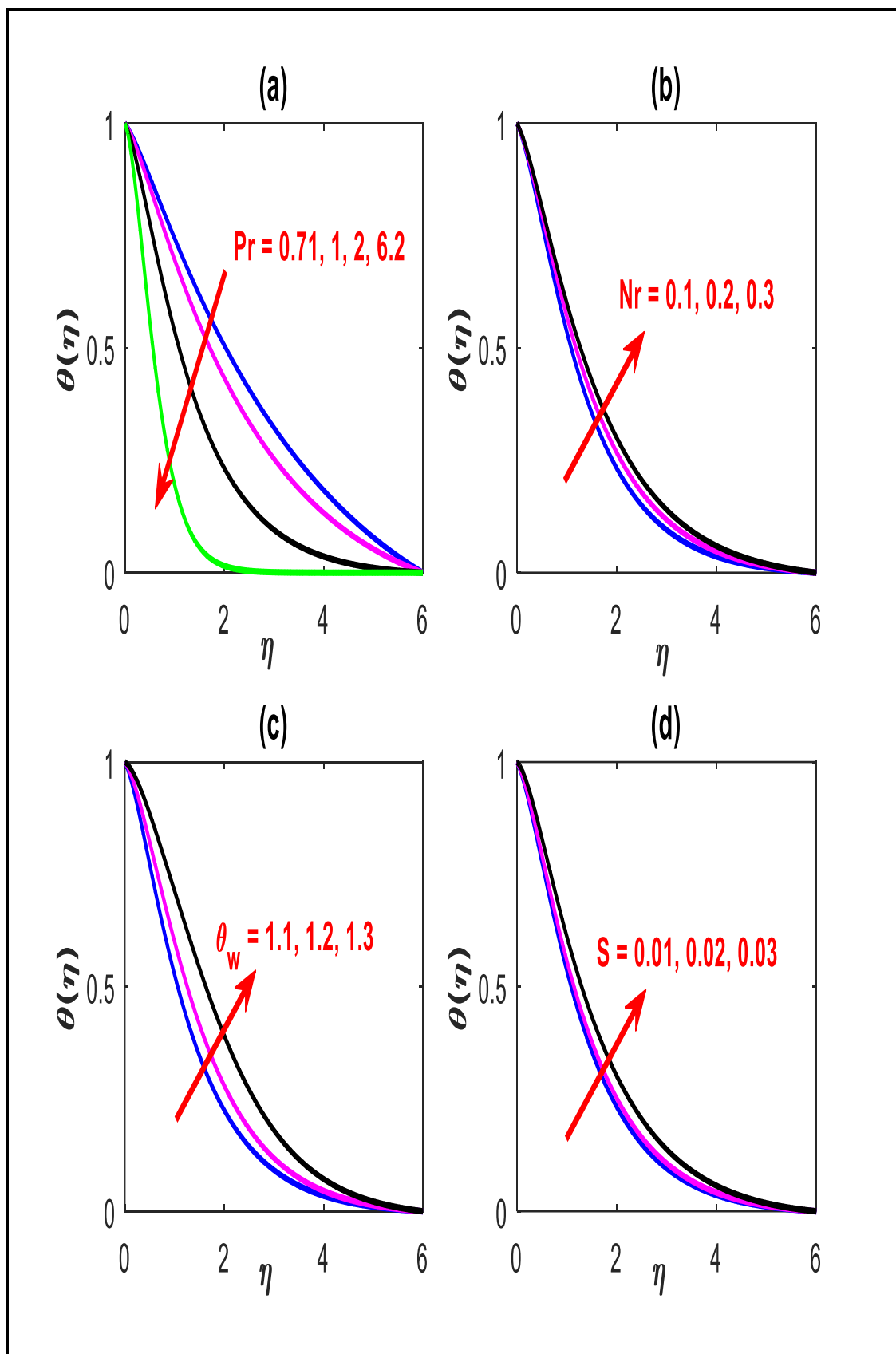
Fig. 5 Evolution of temperature with transverse coordinate for (a) Prandtl number (b) radiative conductive Boltzmann number (c) temperature ratio parameter and (d) heat source (generation) parameter.
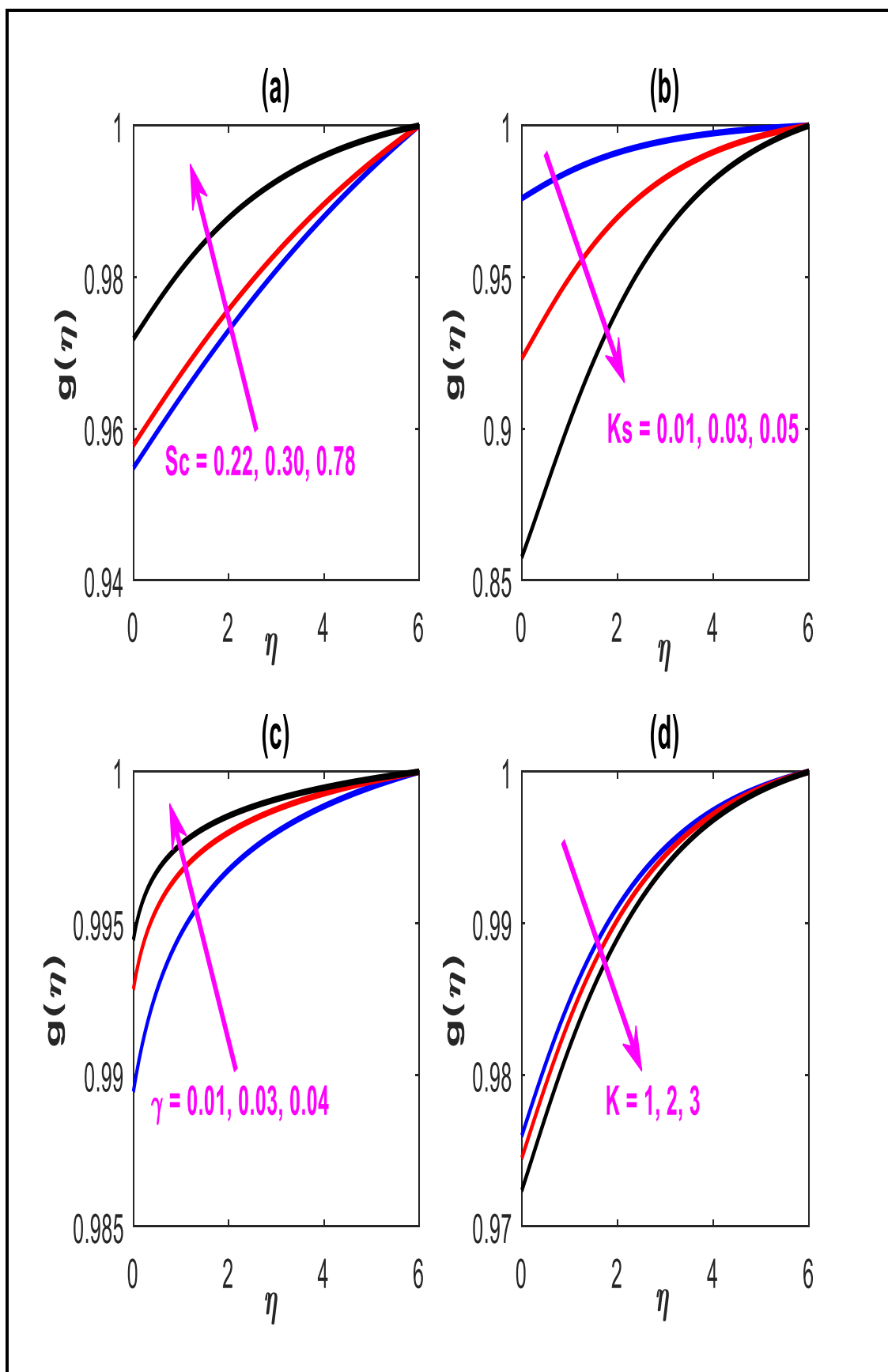
Fig. 6 Evolution of species A concentration $g(\eta)$ with transverse coordinate for (a) Schmidt number (b) heterogenous reaction parameter (c) curvature parameter and (d) homogenous reaction parameter
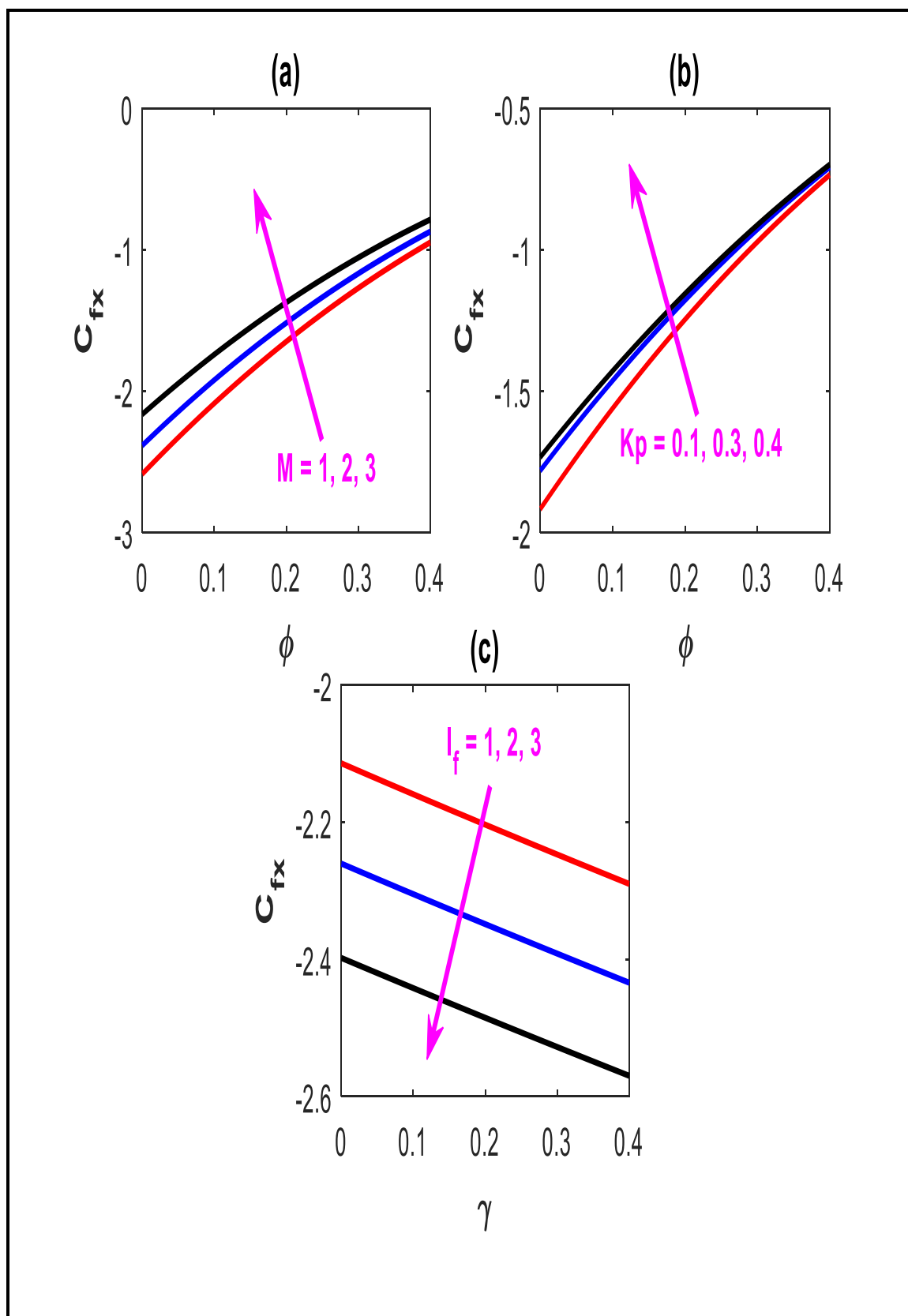
Fig. 7 Variation of skin friction with (a) nanoparticle volume fraction and magnetic Stuart number (b) nanoparticle volume fraction and Darcy parameter and (c) curvature parameter and Forchheimer inertial drag parameter
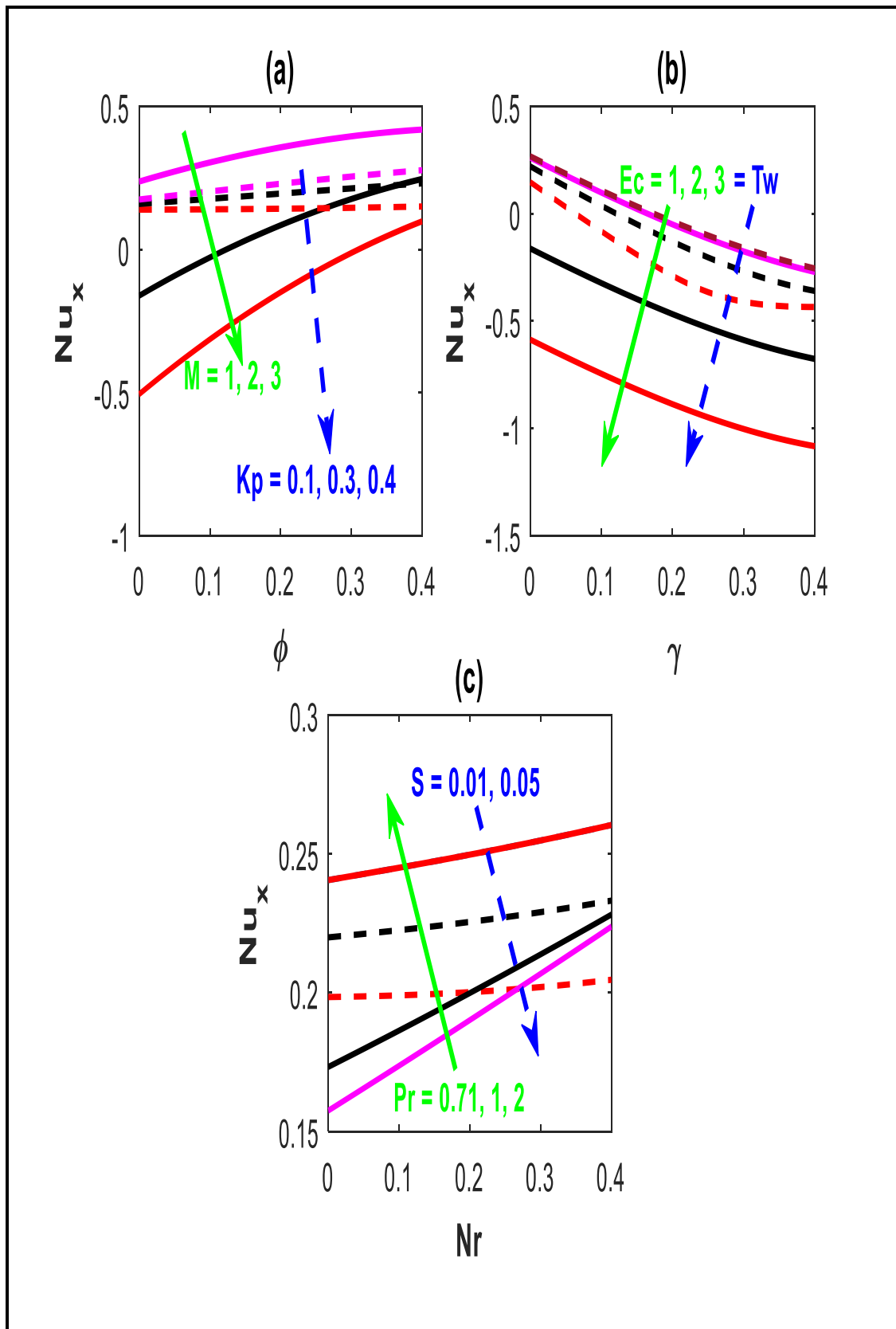
Fig. 8 Variation of local Nusselt number with (a) nanoparticle volume fraction, magnetic Stuart number and Darcian parameter (b) curvature parameter, Eckert number and wall temperature ratio and (c) radiative conductive Boltzmann number, heat source parameter and Prandtl number.
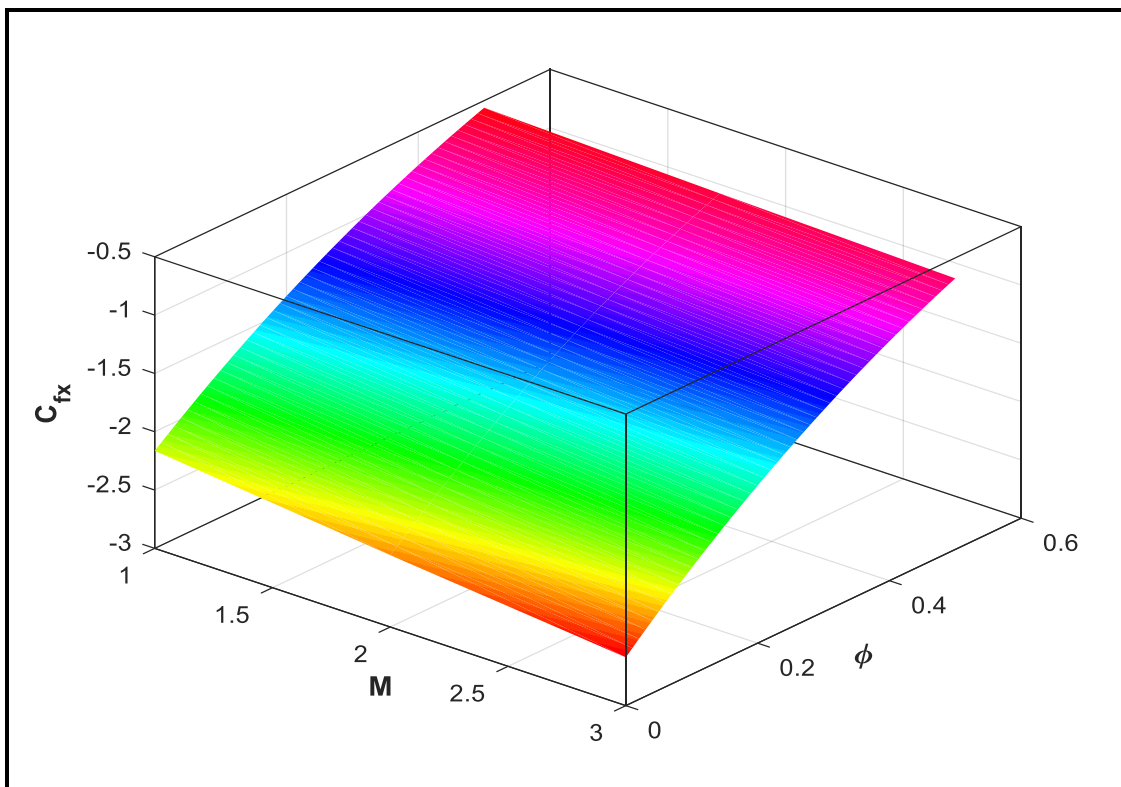
Fig. 9 Contour plot for local skin friction variation with Stuart magnetic interaction number and nanoparticle volume fraction
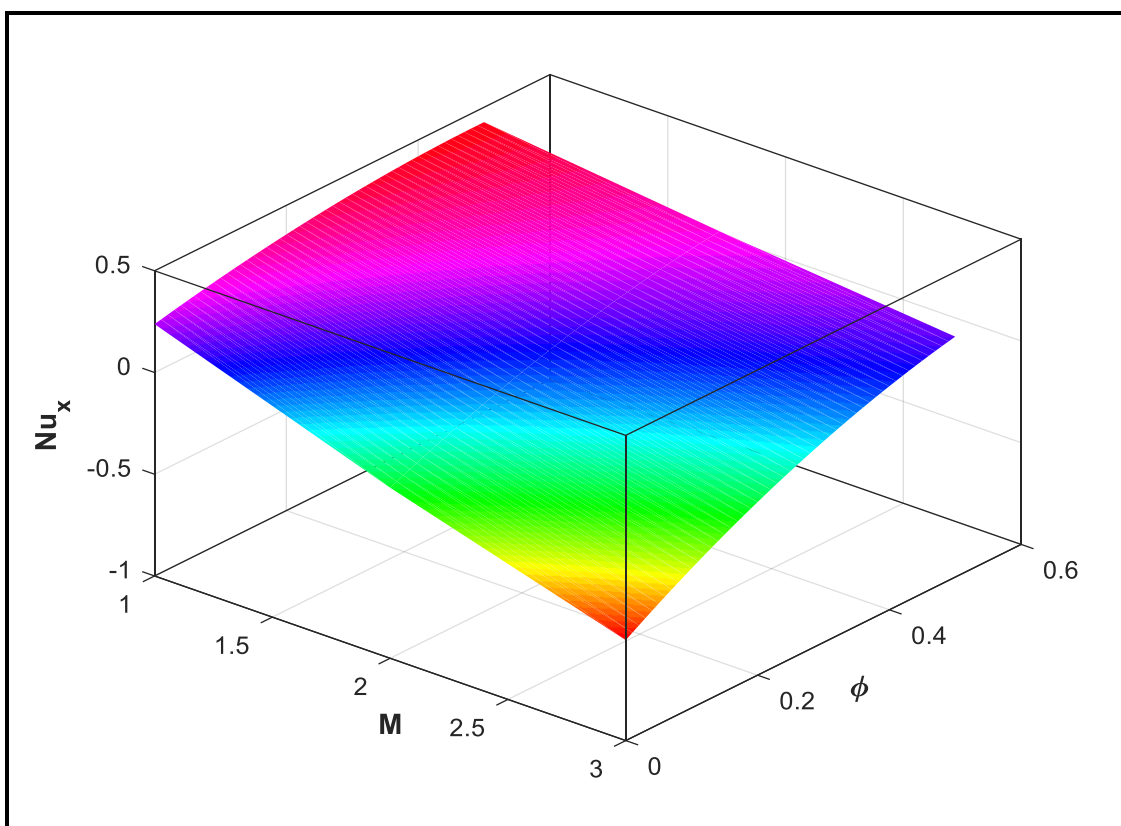

Fig. 10 Contour plot for local Nusselt number variation with Stuart magnetic interaction number and nanoparticle volume fraction

Fig. 11 Contour plot for local skin friction variation with cylinder curvature parameter and Prandtl number

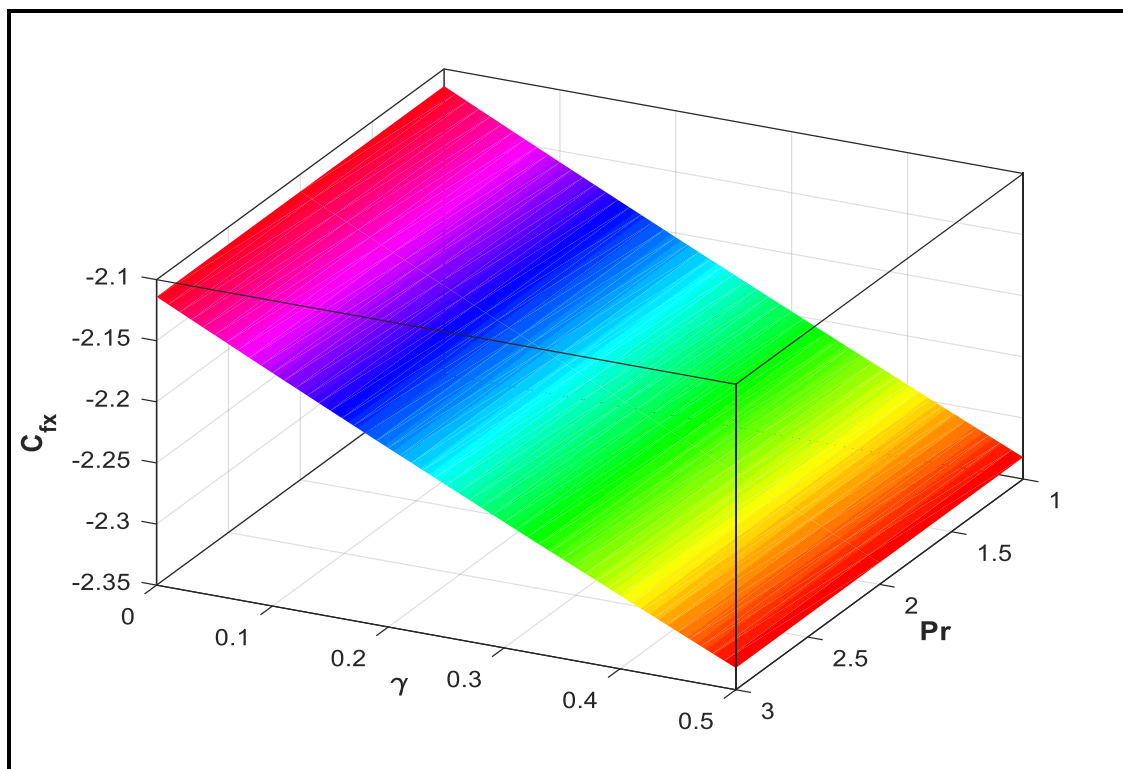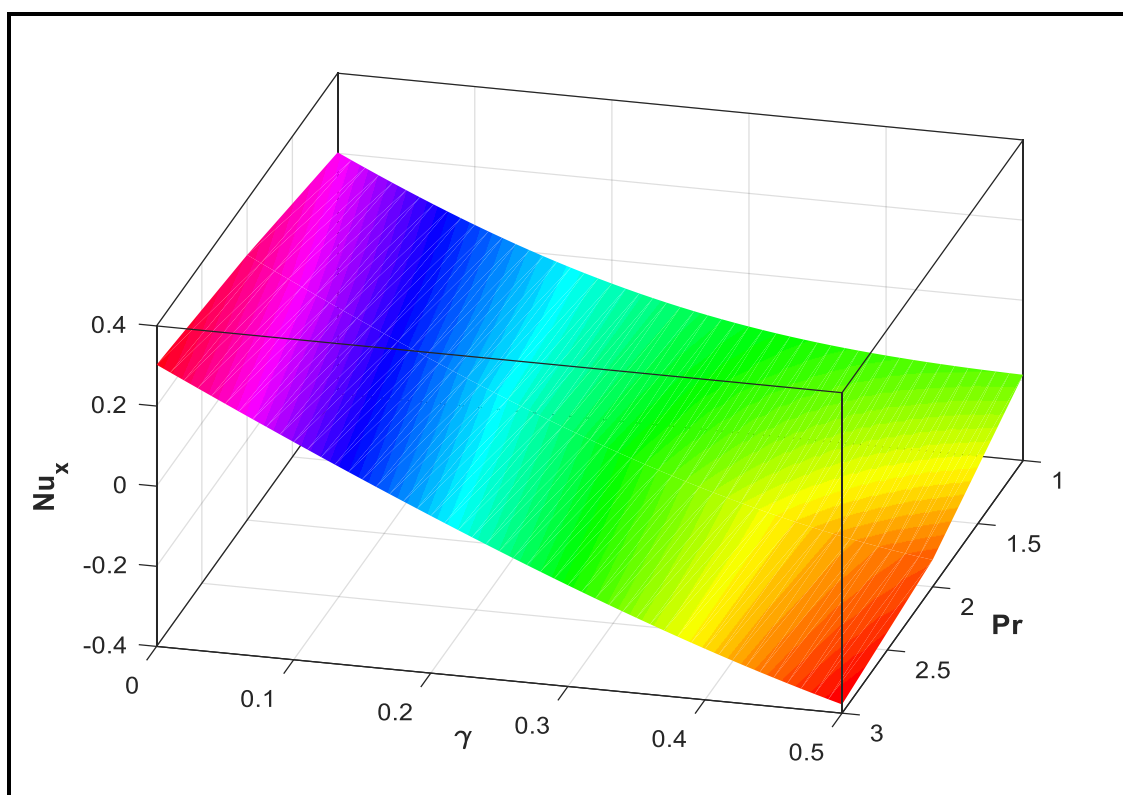**Fig. 12** Contour plot for local Nusselt number variation with cylinder curvature parameter and Prandtl number
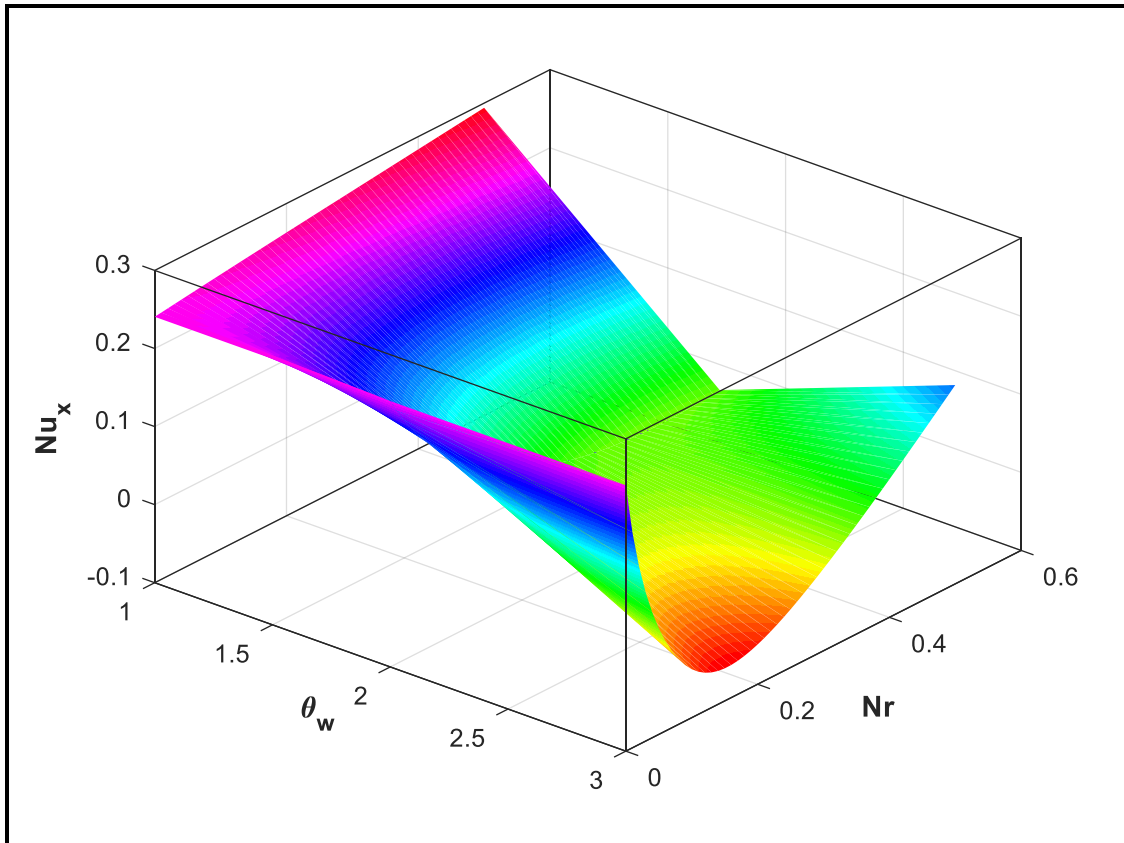
Fig. 13 Contour plot for local Nusselt number variation with temperature ratio parameter and radiative-conduction number (Boltzmann number)
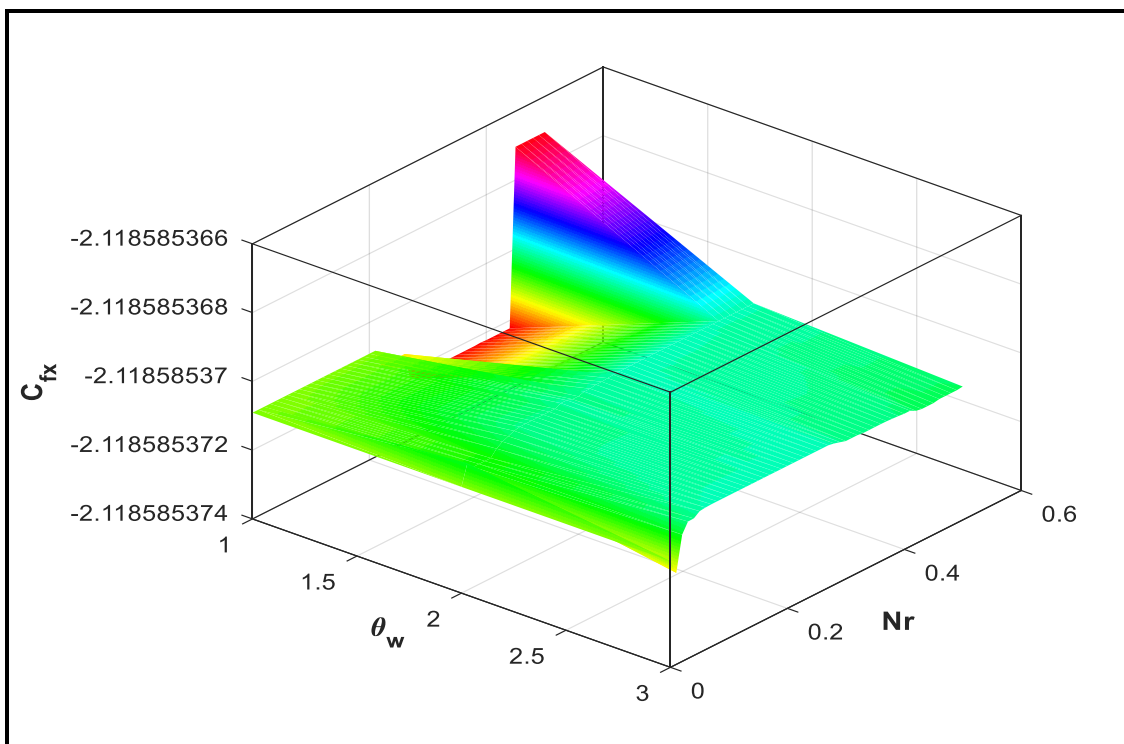
Fig. 14 Contour plot for local skin friction variation with temperature ratio parameter and radiative-conduction number (Boltzmann number)
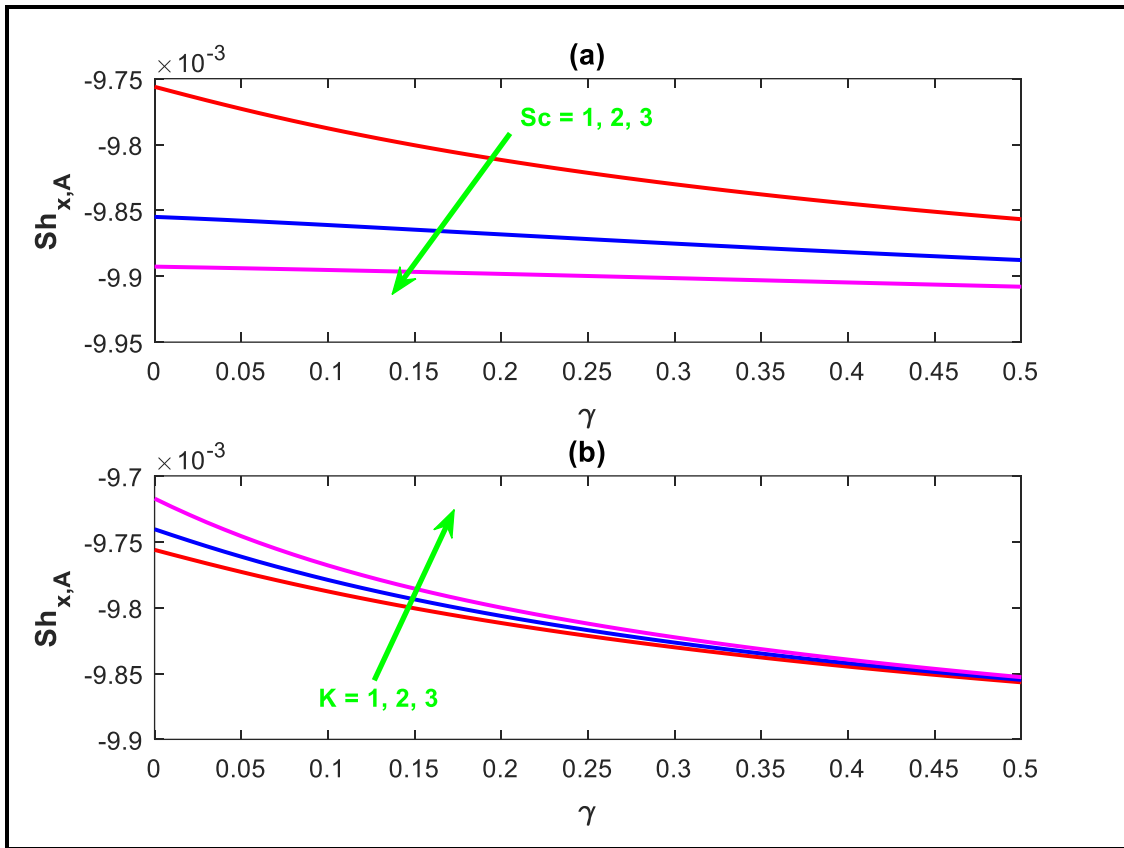
Fig. 15 Variation of local Sherwood number for Species A
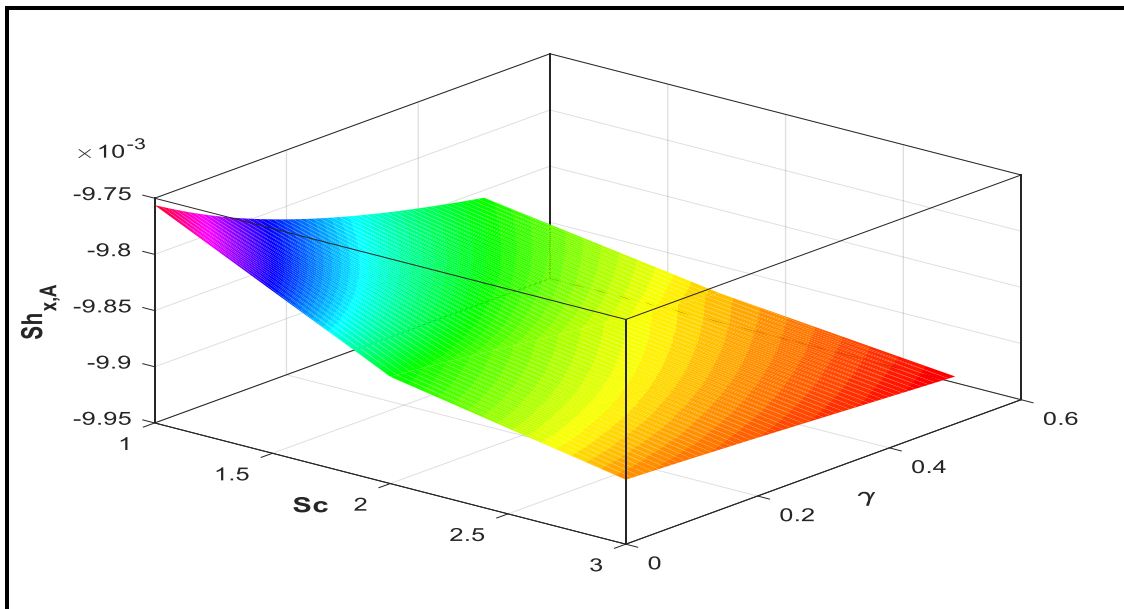
Fig. 16 Contour plot for local Sherwood number variation of species A with Schmidt number and cylinder curvature parameter
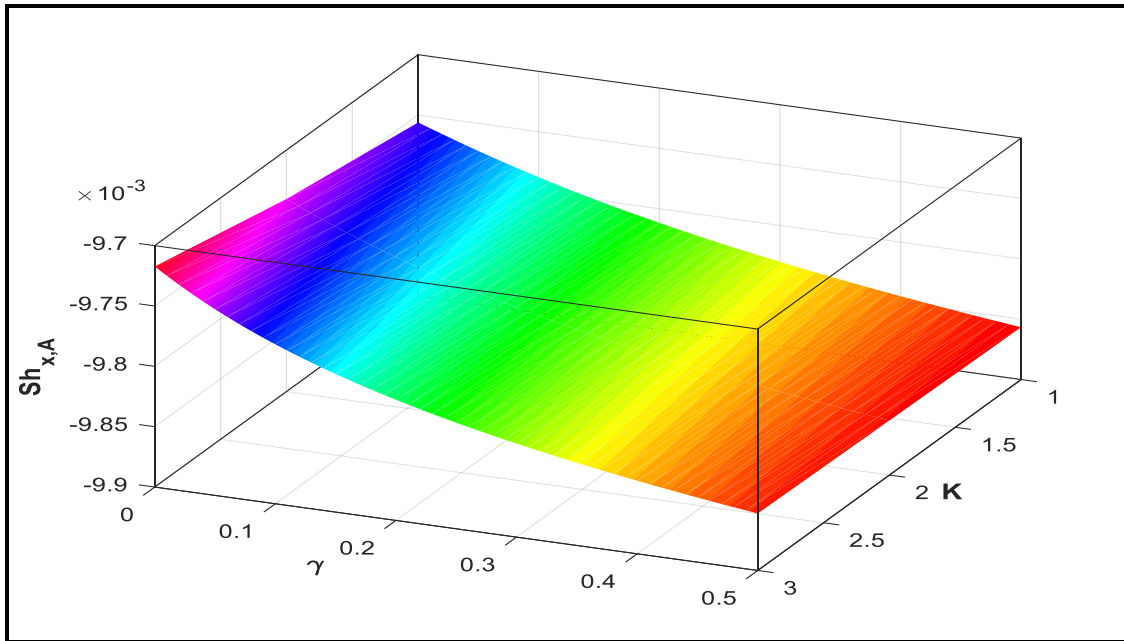
Fig. 17 Contour plot for local Sherwood number variation of species A with cylinder curvature parameter and homogenous reaction parameter
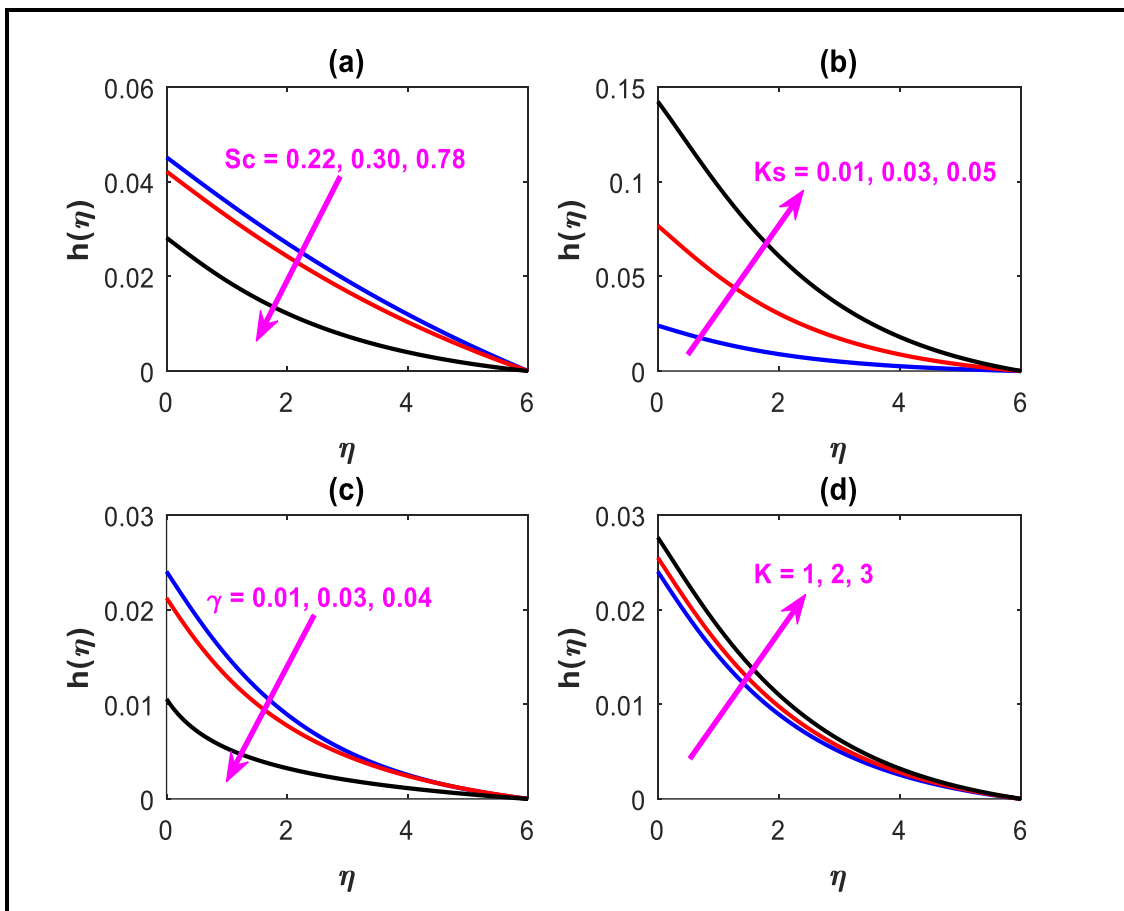
Fig. 18 Evolution of species B concentration profiles $h(\eta)$ with transverse coordinate for (a) Schmidt number, (b) heterogenous reaction parameter, (c) curvature parameter and (d) homogenous reaction parameter.
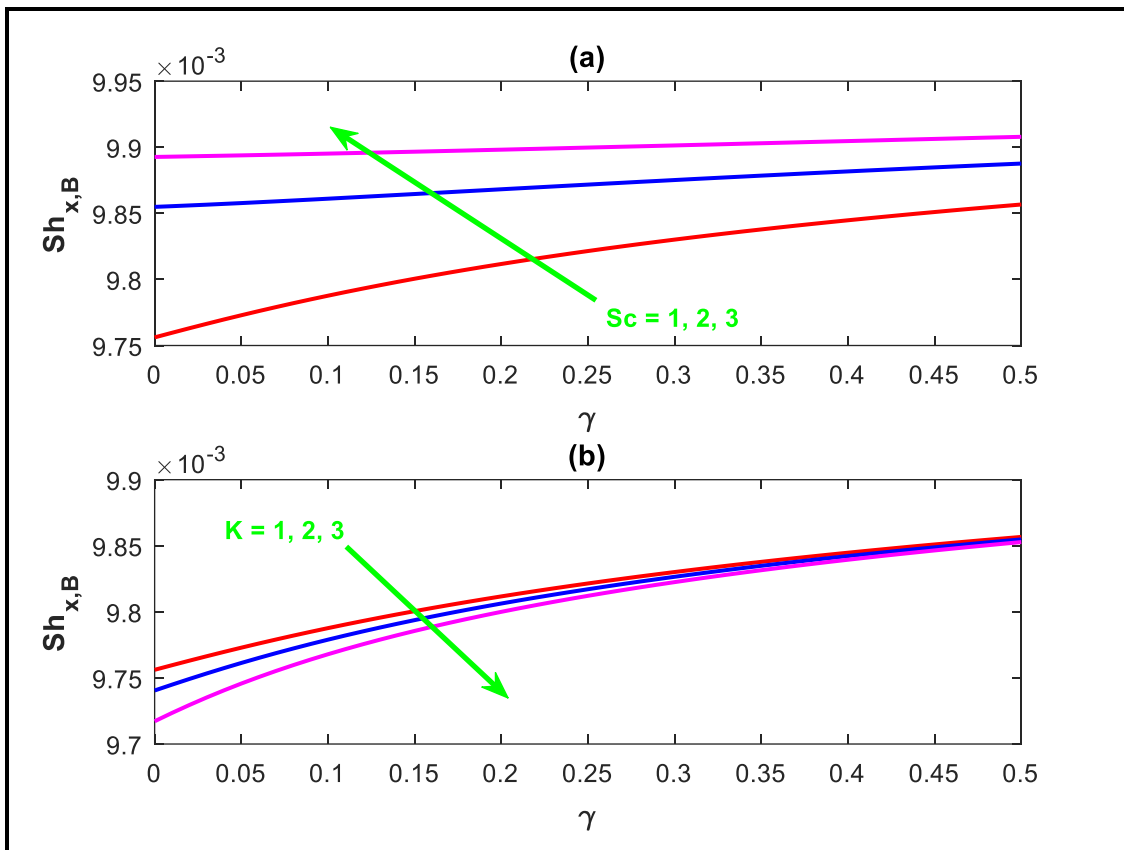
Fig. 19 Evolution of species B local Sherwood number versus curvature parameter for a) Schmidt number (b) homogenous reaction parameter.
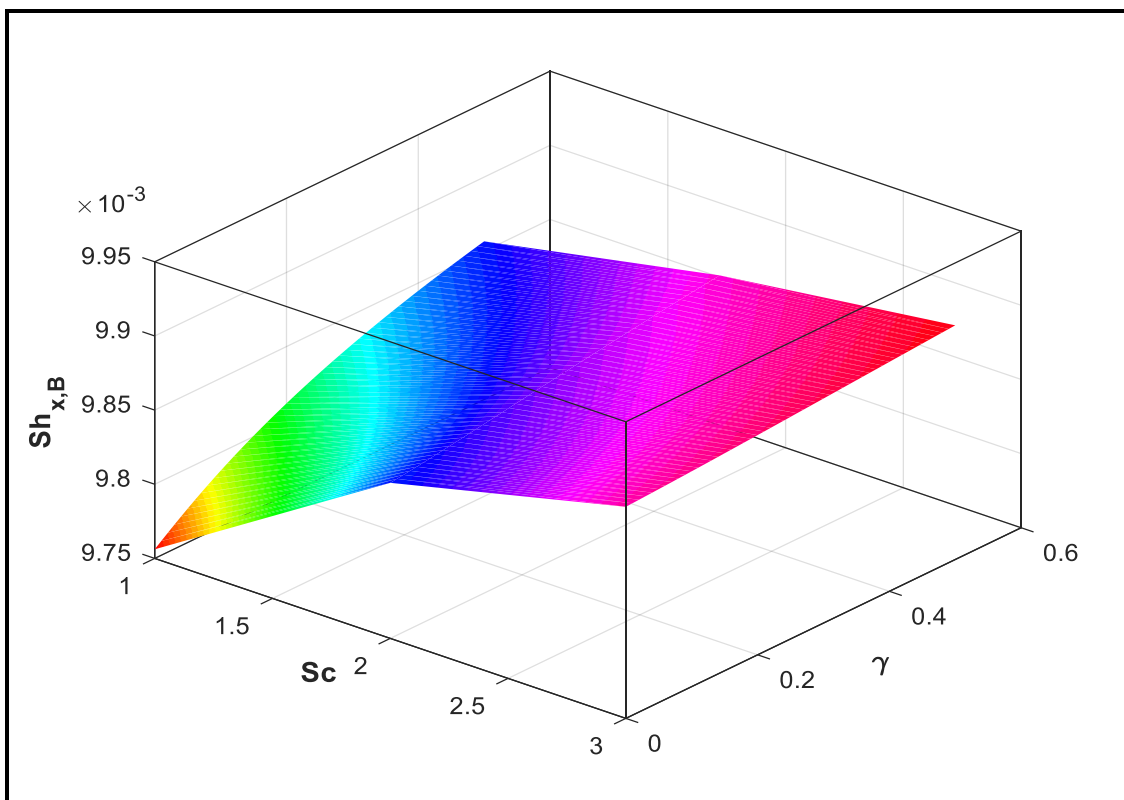
Fig. 20 Contour plot for species B local Sherwood number versus Schmidt number and curvature parameter
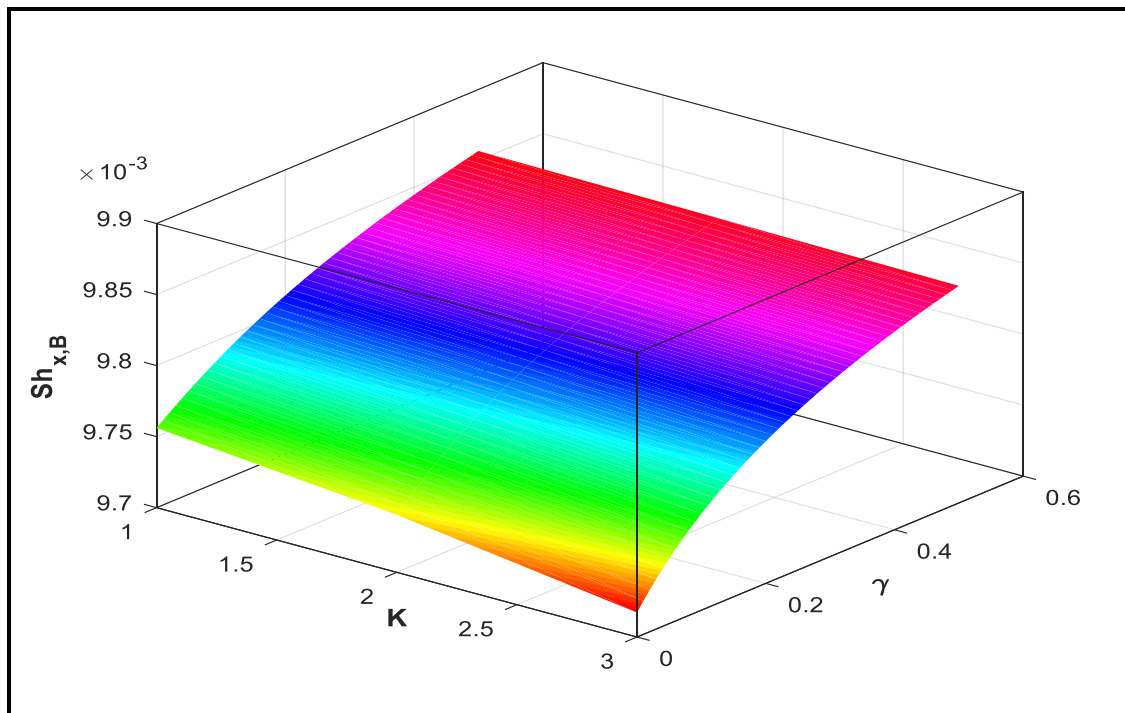
Fig. 21 Contour plot for species B local Sherwood number versus homogenous reaction parameter and curvature parameter

Figs. 3a-d, illustrate the evolution in velocity of the coating boundary layer with distance transverse to the cylinder surface, for (a) nanoparticle volume fraction (b) curvature parameter (c) magnetic Stuart number and Darcian parameter (d) Forchheimer inertial porous media parameter. With elevation in volume fraction, ϕ, as seen in fig. 3a, there is a progressive reduction in velocity. The flow is therefore decelerated with higher volume fraction since the viscosity of the nano-coating is elevated. This implies an improved flow control of the coating deposition during stretching with nanoparticles. Asymptotically smooth decays in velocity from the cylinder surface to the free stream are computed, confirming the prescription of an adequately large infinity boundary condition. The maximum velocity at the cylinder surface i.e. interface between the substrate cylinder and the polymer coating is due to the axial stretching effect which modifies the conventional no-slip wall condition. With higher curvature parameter ($\gamma = \sqrt{\frac{l v_f}{u_0 a^2}}$) as visualized in fig. 3b, a *strong acceleration* is induced in the regime i.e. velocity is boosted and this is particularly prominent at intermediate distance transverse to the cylinder surface; with further progression towards the edge of the boundary layer the profiles become indistinguishable indicating the negligible effect of curvature far from the cylinder surface. When $\gamma = 0$ *curvature effect is negated*. This parameter features in all the

boundary layer Eqns. (12)-(15) but is absent in the boundary conditions (16). However, for progressively smaller values of this parameter the effect is amplified. It is observed therefore that stronger curvature induces a boost in momentum in the stretching coating flow and that despite the more curved nature of the periphery of the substrate, there is never any flow separation produced i.e. velocities are sustained as positive for all values of transverse coordinate. Although in turbulent boundary layer flow, stronger curvature manifests in deceleration, in laminar boundary layers there is a favourable gradient sustained on the cylinder surface which counteracts the retarding effect of the shear stress (which is due to viscosity) in the boundary layer. This generates flow acceleration. The momentum boundary layer thickness is therefore reduced (in turbulent flows the adverse pressure gradient is present which depletes the velocity near the wall and thickens the momentum boundary layer. Similar results have been computed in Qayyum *et al.* [71] although very little, if any, physical insight has been given in that study of any relevance to engineering coating dynamics. Fig. 3c shows that with a progressive increase in magnetic interaction parameter i.e. Stuart number ($M = \frac{\sigma_f a B_0^2}{\rho_f u_0}$) there is a strong suppression in velocity. The radial magnetic field generates a transverse (axial) Lorentzian magnetohydrodynamic drag force. The axial flow is markedly damped therefore with stronger magnetic Lorentz force relative to inertial (momentum) force. This regulates the coating deposition on the cylinder surface and the nano-polymer in this sense is therefore a functional material responding to external field effects. For the case of $M = 1$ both forces contribute equally. For $M > 1$ naturally the magnetic drag force exceeds the inertial force. However, since $M = 3$ is the maximum magnitude considered, the magnetic field is insufficient in intensity to mobilize Hall currents and is therefore "weak". Nevertheless, the desired objective of thickening the momentum boundary layer is achieved. The Darcian parameter, Kp, simulates the linear drag effect of the bulk porous media fiber resistance at low Reynolds number on the coating nano-polymer. It appears as a reciprocal parameter in the momentum boundary layer Eqn. (12), viz, $-\left(A_2 K_p^{-1}\right) f'$. $Kp = \frac{u_0 K_p^*}{v_f a l}$ i.e. is directly proportional to the actual permeability of the medium. With greater values of Kp there will therefore be a reduction in Darcian impedance i.e. less resistance to the nano-polymer will be offered by the medium and this will induce *axial flow acceleration*. This explains the profiles in fig. 3a. Of course, in the limit when $Kp \to \infty$ (and of course when Forchheimer quadratic drag parameter, I_f, $\to 0$) the solid fibers vanish and the regime is purely nano-polymer fluid. Fig. 3d shows that with increasing Forchheimer quadratic drag parameter, $I_f = \frac{x a I^*}{\mu_f \sqrt{Kp^*}}$ there is a significant depletion

in the axial velocity, f'. The Forchheimer second order drag term also appears in the momentum boundary layer Eqn. (12) in the form, $-A_1(I_f f'^2)$. Although this body force increases with inertial effect i.e. greater Reynolds number, it is not associated with acceleration of the flow. the overwhelming effect of quadratic drag is to decelerate the blood flow in the porous regime. This is characteristic of Forchheimer effects and has been computed in numerous other studies including Vafai and Tien [51] and Dybbs and Edwards [52]. As noted earlier the purely fluid (nano-polymer) regime scenario is retrieved for $Da \rightarrow \infty$ and $I_f = 0$. The Darcy drag force arises from the viscous contribution to stress at the solid particle boundaries. As such with increasing permeability (and Da value) the flow receives progressively less resistance from the porous fibers which diminish in concentration. Inertial effects due to the porous medium are experienced via the quadratic drag term i.e. Forchheimer term which does not explicitly involve viscosity but does arise from viscosity action, mediated by the inertial effects affecting the distribution of pressure which also contributes to the stress at the solid boundary i.e. vessel wall. Forchheimer drag, as shown by Joseph *et al*. [53] models essentially a form drag phenomenon, and in fact involves the separation of boundary layers and wake formation behind solid obstacles (solid matrix fibers, bundles etc). The pore scale convective inertial effects contributing to the form drag lead to a substantial alteration of the velocity field and exacerbate the macroscopic region in which the pore scale velocity gradients are large. Lage [54] has effectively shown that these characteristics apply to both porous media of the bluff body type as well as those of the conduit type (relevant to the present model). Skejtne and Auriault [55] have further indicated that Forchheimer drag simulates the strong inertial flow regime in porous media hydrodynamics. This pertains to the regime where the pore Reynolds number, based on a consideration of the particle or pore diameter, is greater than or equal to unity. At this point the model departs from the purely Darcian or viscous-dominated classical porous media transport physics. It is also pertinent to note that the range of I_f values considered up to 4 does not stimulate *vortex formation* associated with higher Reynolds numbers (greater than 250). However, the boundary layers around the pores become more pronounced and an "inertial core" appears with higher Forchheimer number. The developing of these "core" flows external to the boundary layers accounts for the *non-linear relationship* between pressure drop and flow rate. Strong regulation of the coating velocity field therefore is achievable by pressure generated inertial effects in the porous medium (these can be achieved with industrial fans or blower devices, as popularized by Mitsubishi corporation, Japan).

Fig. 4 illustrates the distribution of dimensionless temperature with transverse coordinate for (a) nanoparticle volume fraction (b) curvature parameter (c) magnetic Stuart number and Darcian parameter (d) Eckert number. Increasing volume fraction of Titanium dioxide nanoparticles (fig. 4a) clearly decreases temperatures within the coating layer, since it encourages heat diffusion to the wall. This response is sustained throughout the boundary layer transverse to the cylinder surface (wall). Thermal boundary layer thickness is therefore suppressed with greater nanoparticle fraction, an important feature of metallic nano-doped polymers, as noted by Das *et al.* [20]. Therefore the thermal enhancement features of metallic nanoparticles achieve a cooling of the polymer coating by transferring heat via higher thermal conductivity of Titanium dioxide compared to the base polymer (polymers generally have high Prandtl numbers and are efficient thermal insulators not thermal conductors). Increasing curvature parameter, γ, (fig. 4b) is found to marginally energize the coating i.e. increase temperatures. Thermal boundary layer thickness is weakly increased. However, the effect is much less dramatic than the alteration in the axial velocity distribution (fig. 3b). The pressure gradient therefore has the *secondary* influence of encouraging heat diffusion in the nano-polymer with more curved cylinder topology. Fig. 4c exhibits a strong elevation in temperature with an increase in Stuart magnetic interaction parameter, *M*. Owing to the presence of Ohmic dissipation i.e. Joule electrical heating, magnetic parameter features in the energy conservation Eqn. (13) in the term, $+A_3 M Ec(f'^2)$. There is also strong coupling of the temperature field (θ) terms with the momentum Eqn. (12) e.g. $+A_5 f \theta'$, there is a strong interplay between heat and momentum transfer. The elevation in temperature is generated by the dissipation in supplementary work expended in dragging the nano-polymer against the action of the magnetic field, as thermal energy. This manifests in an increase in thermal boundary layer thickness along the cylinder surface. The classical parabolic decay in temperature from the cylinder surface to the free stream is observed irrespective of whether magnetic effect is present or not. However, with an increase in Darcy parameter (*Kp*), the temperature is depressed in the regime. The higher permeability implies a depletion in solid fibres. This inhibits thermal conduction heat transfer between the particles in the percolating nano-polymer and results in a cooling of the regime and decrease in thermal boundary layer thickness. More permeable media are therefore more conducive to heat regulation in the coating process whereas more densely packed porous media (lower permeability) induce the reverse effect. Fig. 4d indicates that with increasing Eckert number, *Ec,* there is an enhancement in temperature. $Ec = \frac{u_0 x^2}{(\rho c_p)_f T_\infty (\theta_w - 1)}$ signifies viscous heating effect in the nano-polymer. Viscous heating has been confirmed to be

a very significant phenomenon in polymer coating dynamics which should not be ignored. Eckert number embodies the ratio of the kinetic energy dissipated in the flow to the boundary layer enthalpy difference. For $Ec > 0$, heat moves away from the cylinder surface to the boundary layer. A substantial enhancement in thermal boundary layer thickness is generated with greater Eckert number. The implication is that neglection of this effect in thermo-magnetic nano-coating models leads to an under prediction in temperatures in the boundary layer i.e. less accuracy in characterizing thermal distribution (which is critical in manipulating global properties of the nano-polymer) is possible with non-dissipative mathematical flow models.

Fig. 5 depicts the variation in temperature with transverse coordinate (η) for (a) Prandtl number (b) radiative conductive Boltzmann number (c) temperature ratio parameter and (d) heat source (generation) parameter. Fig. 5a shows that with elevation in Prandtl number P_r leads to a strong reduction in temperature distribution. "P*randtl number is inversely proportional to effective thermal conductivity of the magnetic nano-polymer*". When $Pr = 1,$ both momentum and thermal boundary layer thickness are of the same order of magnitude. $Pr = 1, 2$ corresponds to aqueous magnetic nano-polymers which combine the low Prandtl number ($<< 1$) of metallic nanoparticles (Titanium dioxide) with the higher Prandtl number of water ($Pr \sim 6$). As Pr is increased, thermal conductivity retards. "The heat transported by molecular conduction is therefore suppressed which manifests in a decrease in temperatures and a depletion in thermal boundary layer thickness. Cooling of the stretching coating regime is therefore achieved with higher Prandtl number whereas heating is observed with lower Prandtl numbers. Prandtl number also relates the momentum diffusion rate and the thermal diffusion rate. As Prandtl number increases (beyond unity) the momentum diffusion rate greatly exceeds thermal diffusion rate which results in a suppression of thermal diffusion and lower temperatures[61]". Fig. 5b shows that with increasing radiation-conduction (Boltzmann) number, *Nr,* there is a significant enhancement in temperatures. $Nr = \frac{16\sigma^* T_\infty{}^3}{3k^* k_f}$ and appears in the augmented thermal diffusion term in Eqn. (13), viz $\frac{1}{Pr} Nr (1 + (\theta_w - 1)\theta)^3$. When $Nr = 0$ radiative effects vanish, and the regime is conduction-dominated based on the Fourier conduction law. With increasing Nr values there is a progressive boost in the uni-directional (radial) radiative heat flux applied to the cylinder coating. This energizes the boundary layer and increases thermal boundary layer thickness. Even a slight modification in radiative parameter exerts a marked influence on heat transfer characteristics across the boundary layer transverse to the stretching cylinder surface. The neglection of radiative effects in high temperature materials processing

therefore severely under-predicts actual temperatures in the coating material. This will also lead to erroneous results in Nusselt number (wall heat transfer gradient) computation. The *Rosseland diffusion flux model* therefore, while simple and restricted to optically dense media (magnetic nano-polymers) however does successfully capture general radiative heat transfer effects in materials processing systems. The current simulations also provide a good platform for extension of the current model to more sophisticated radiative flux models such as the Chandrasekhar discrete ordinates model or the Traugott P1 differential flux model as elaborated by Bég *et al.* [61]. Inspection of Fig. 5c reveals that with temperature ratio parameter (θ_W). This parameter arises solely in the energy Eqn. (13) and is defined as $\theta_w = \frac{T_w}{T_\infty}$. There is a substantial enhancement in temperature in the nanocoating boundary layer. Thermal boundary layer thickness is also elevated since prescribed surface temperature (T_W) exceeds the free stream temperature at the edge of the boundary layer regime. Heat is therefore transferred efficiently from the cylinder surface into the boundary layer coating regime; this energizes the flow. Fig. 5d visualizes the impact of heat source on the temperature field. This may be generated with for example a laser heating source on the cylinder coating to modify the polymer viscosity via entanglement re-adjustment on the molecular level, as noted by Viskanta [32]. This serves as a supplementary effect to thermal radiation and is a useful technique for manipulating thermal diffusion in polymer stretching coating dynamics [64]. Even with a minor increment in the heat source parameter, *S*, there is a notable accentuation in the temperature in the boundary layer. Heating is therefore prominent with a laser source and thermal boundary layer thickness is enhanced in the coating on the cylinder.

Fig. 6 depicts the distribution in reactive species A concentration $g(\eta)$ with transverse coordinate (η) for (a) Schmidt number (b) heterogenous reaction parameter (c) curvature parameter and (d) homogenous reaction parameter. The mass diffusion of primary species, *A* (oxygen) is described by the normalized species *A* boundary layer Eqn. (14). Fig. 6a shows that with an increase in Schmidt number (Sc), there is a dramatic elevation in species A concentration magnitude, $g(\eta)$. All profiles grow steadily from the cylinder surface to the free stream. However, for very low *Sc* values (0.22 which may represent *oxygen diffusing in lower-viscosity highly aqueous functional polymer*) the ascent is *linear in nature* whereas for higher *Sc* (0. 3, 0.78 which respectively represent hydrogen and nitrogen diffusing in magnetic nano-polymer) the profiles assume a parabolic monotonic growth disposition. Schmidt number $Sc = \frac{v_f}{D_A}$ embodies the ratio between momentum and mass diffusivity of species B. It is evident that

increasing Schmidt number tends elevates concentration magnitudes markedly and this trend is sustained throughout the boundary layer transverse to the cylinder surface. For gaseous diffusion in polymers, $Sc < 1$ and the momentum diffusion rate is exceeded by the species diffusion rate and higher concentration magnitudes are computed. Conversely when $Sc > 1$ the momentum diffusion rate exceeds the species diffusion rate and this will produce a depression in concentration values. For the case of $Sc = 1$ both momentum and nano-particle species diffusion rates are equivalent as are the boundary layer thicknesses. Species A concentration boundary layer thickness is clearly elevated as Sc increases from 0.22 through 0.3 to 0.78. The diffusivity of oxygen molecular species A in the nano-polymer therefore critical to how effectively oxygen can move in the functional polymer and reaction rates. It is noteworthy that the species diffusion is assumed to obey Fickian diffusion, although in the future non-Fickian diffusion, which has also been reported in smart coating, may be examined. Fig. 6b demonstrates that with increasing heterogenous reaction parameter (Ks) there is a marked suppression in concentration magnitudes. $K_S = \frac{k_s^*}{D_A}\sqrt{\frac{v_f l}{u_0}}$ and arises in the wall boundary conditions (16). It is associated with the *first order, isothermal catalytic reaction at the substrate (cylinder) surface*, as defined in the autocatalytic reaction Eqn. (2) i.e. $A + B \rightarrow 3B$, $rate = \text{Ks}\chi$. *Ks* therefore does not feature in the species diffusion A conservation Eqn. (14) but appears in the wall boundary conditions, $g' = K_s g, \delta h' = -K_s g$ at $\eta = 0$. Minimum concentrations associated with this heterogenous destructive reaction are therefore present at the cylinder surface since here the maximum conversion of species A to a new species is produced. Species A concentrations ascend from the wall to the free stream where they are naturally a maximum at the greatest distance from the cylinder surface. As Ks increases the concentration magnitudes of species A (molecular oxygen) are suppressed since more and more species A is destroyed. All profiles asymptotically converge to the free stream confirming the imposition of an adequately large infinity boundary condition in the simulations. Fig. 6c indicates that an increment in curvature parameter (γ) there is a considerable elevation in the species A concentration $g(\eta)$. Concentration boundary layer thickness for molecular oxygen (A) is also enhanced. As noted earlier the pressure gradient in the coating flow assists momentum diffusion with greater curvature of the cylinder surface. All profiles are monotonic growths from the cylinder wall to the freestream. Steady responses are computed, as with temperature and velocity; no instability in the regime is induced even at high curvatures. The curvature is related to the diameter of the coated substrate. Larger curvature corresponds to

small diameter cylinders and vice versa for smaller curvature. The implication is that stable coating deposition is achieved via stretching over a range of cylinder sizes (diameters). Of course the analysis is confined to laminar flow which is the attraction of stretching coating systems, as opposed to spray deposition processes which while faster are inherently turbulent and do not achieve the same degree of homogeneity of the coatings [75]. Spray coating usually employs thermal (flame) deposition technology for metallic-based coatings. However, stretching techniques have been shown to achieve enhanced control and efficiency with practically no wastage of materials [76]. Fig. 6d reveals that a strong decrement in species *A* concentration $g(\eta)$ accompanies an increase in the homogenous reaction parameter, $K = \frac{a_0^2 l k_1}{u_w}$. This parameter arises in the species A/B coupling term, $-Kgh^2$ in Eqn. (14). There is a corresponding cross link term in the species B (hydrogen) boundary layer equation (15), viz $+Kgh^2$. However the polarity of these terms is evidently opposite. In the case of the species A (oxygen), the term is destructive (negative), whereas in the case of species B it is constructive (positive). A sharp ascent in species A concentration profiles is observed with increasing transverse coordinate i.e. with progressive distance from the cylinder surface species A concentration magnitudes are elevated, and this has been explained in earlier.

Fig. 7 visualizes the evolution in cylinder surface skin friction, C_{fx}, with (a) nanoparticle volume fraction and magnetic Stuart number (b) nanoparticle volume fraction and Darcy parameter and (c) curvature parameter and Forchheimer inertial drag parameter. Fig. 7a) illustrates the evolution of skin friction with (a) nanoparticle volume fraction and magnetic Stuart number (b) nanoparticle volume fraction and Darcy parameter and (c) curvature parameter and Forchheimer inertial drag parameter. Skin friction is a critical design parameter in coating dynamics and is found to be enhanced with greater magnetic Stuart number. Flow at the interface between the coating and cylinder surface s therefore accelerated with greater magnetic field intensity, whereas velocity *within the boundary layer* is reduced (Fig. 3b). There is also a progressive elevation in skin friction with increasing volume fraction. Similarly, fig. 7b shows that with both Darcy parameter, *Kp* and volume fraction, ϕ, there is an enhancement in skin friction. A greater permeability of the porous material and higher percentage of doping in the functional nano-polymer with Titanium dioxide nanoparticles accelerates the flow at the cylinder surface i.e. the nano-polymer shears faster along the surface. Conversely in fig. 7c is t is evident that greater Forchheimer inertial parameter, I_f, and cylinder curvature both deplete the skin friction. Therefore, with amplification in inertial effects (higher pore Reynolds

number) in the regime and greater pressure-driven flow through the porous matrix in addition to smaller diameter cylinders, skin friction is supressed.

Fig. 8 depicts the distributions for local Nusselt number, Nu_x, i.e. local heat transfer rate to the wall with (a) nanoparticle volume fraction, magnetic Stuart number and Darcian parameter (b) curvature parameter, Eckert number and wall temperature ratio and (c) radiative conductive Boltzmann number, heat source parameter and Prandtl number. Nusselt number is significantly decreased with greater magnetic interaction parameter (*M*), as observed in Fig. 8a, since the energization of the nano-polymer heats the body of the functional fluid and inhibits heat transport towards the wall. Cooling of the metal substrate (cylinder) is therefore achieved with stronger radial magnetic field and this is beneficial to coating operations since it avoids surface degradation of the substrate via thermal gradients. Similarly, local Nusselt number magnitudes are depleted with increasing Darcian parameter since higher permeability corresponds to sparsity in the solid fibres, reduction in thermal conduction and a concomitant cooling of the cylinder surface (boundary). Fig. 8b shows that the heat transfer rate to the wall is also reduced with both Eckert (viscous heating) number and temperature ratio, since both these quantities are known to heat the boundary layer coating. This increases the *heat transferred away from the cylinder* to the nano-polymer and results in a simultaneous decrease in heat transferred to the cylinder. The increment in Eckert number will also contribute to the Ohmic dissipation i.e. electromagnetic heating of the nano-polymer which reduces heat transferred to the cylinder surface. Fig. 8c shows that with greater heat source effect (*S*), there is an associated depletion in Nusselt number. Heat source increases temperatures within the nano-polymer coating and mitigates the transport of heat to the wall from the fluid. This manifests in a reduction in Nusselt number i.e. cooling of the substrate surface. Conversely with increasing Prandtl number, since the nano-polymer is cooled, heat is successfully conveyed to the cylinder surface i.e. Nusselt number magnitudes are enhanced. As indicated earlier, an elevation in radiative-conduction parameter (Boltzmann number) energizes the nano-polymer and induces heat transport away towards the cylinder surface; effectively therefore local Nusselt numbers are accentuated.

Figs. 9-14 present contour topologies for local skin friction and Nusselt number with variation in selected thermophysical, geometric, magnetic and nanoscale parameters. **Figs. 9, 10** visualize the contour distributions for skin friction and Nusselt number with Stuart magnetic interaction number and nanoparticle volume fraction variation. The computations described earlier are confirmed in these MATLAB plots, which again show that skin friction (Fig. 9) is strongly modified by Stuart number and nanoparticle volume fraction. The relationship is non-linear in both cases. There is a distinct reduction in local Nusselt number (Fig. 10) with

increasing Stuart magnetic number whereas it is significantly enhanced with greater volume fraction of the Titanium dioxide nanoparticles (due to higher thermal conductivity of the metallic component relative to the aqueous polymer base liquid). The potence of the "field control" of functional nano-polymers is therefore strongly evidenced. **Figs. 11, 12** depict the contour distributions for skin friction and Nusselt number with cylinder curvature parameter and Prandtl number. A slight decrease in skin friction (Fig. 11) is associated with increasing Prandtl number, whereas a prominent reduction in skin friction accompanies an increase in cylinder curvature parameter. Fig. 12 also reveals that local Nusselt number is very strongly depleted with greater curvature parameter whereas there is a more significant ascent in local Nusselt number with greater Prandtl number. **Figs. 13, 14** display the contour distributions for skin friction and Nusselt number with increment in temperature ratio parameter and radiative-conduction number (Boltzmann number). More complex topologies are computed in these figures compared with **Figs. 9-12**. Increasing temperature ratio consistently reduces local Nusselt number (Fig. 13); however while *initially there is a reduction in local Nusselt number* with Boltzmann radiative-convective parameter, quickly however, this trend is reversed and a very substantial boost in local Nusselt number is computed at higher values of Boltzmann number (stronger radiative flux contribution). This warps the contour topology into a *saddle point minimum* which is not present in other contour plots (**Figs. 9-12**). There is therefore a double minimum in local Nusselt number computed at high values of temperature ratio and very low values of Boltzmann number. The saddle point is also asymmetric and skewed towards the lower right corner of the plot. Fig. 14 shows that with increasing temperature ratio, *at low and very high values of Boltzmann radiative-conductive number*, there is an elevation in the skin friction at the cylinder surface. However, at high values of Boltzmann number, there is a significant decrease in skin friction magnitudes. A plateau is approached at very high temperature ratios. With increasing Boltzmann number, *Nr*, at very low temperature ratio, the topology is initially invariant, whereas as *Nr* increases, there is a sharp depression in skin friction followed by a much sharper ascent at higher *Nr* values. The insight into this important modification in shearing behaviour at the cylinder surface is only possible with such contour topologies.

Fig. 15 illustrates the response in local Sherwood number for Species A with various parameters. The contour topologies associated with Fig. 15 are subsequently presented in **Figs. 16 and 17**. Fig. 15a shows that with increasing Schmidt number there is a considerable depression in local Sherwood number. Mass transfer rate of species *A* to the wall is quantified by $Sh_{x,A}$. Magnitudes are depleted significantly also with increasing curvature parameter.

Furthermore, profiles also morph from a monotonic decay from zero curvature and low curvature values (at Schmidt number of unity) to more gentle descents for $Sc > 1$, indicating that a nonlinear relationship exists in the former and a linear one in the latter. Mass diffusivity of species in combination with cylinder curvature therefore both contribute to modification in the rate of mass transfer of reactive species A to the cylinder boundary. In all cases maximum $Sh_{x,A}$. arises for zero curvature (for which the cylinder becomes a *perfectly flat steel substrate surface*). Inspection of Fig. 15b shows that a consistently monotonic decay in local Sherwood number, $Sh_{x,A}$ accompanies an increase in curvature parameter, irrespective of the value of homogenous chemical reaction parameter, K. With greater K values the intensity of the homogenous chemical reaction *within the bulk of the nano-polymer coating*, as distinct from the boundary chemical reaction (Ks) the magnitudes of $Sh_{x,A}$ are substantially boosted. The decrease in species A induced with intensification in the chemical reaction rate (K) i.e. bulk reaction, depletes the concentration of molecular oxygen (species A) in the nanopolymer coating. This encourages mass transfer to the wall (cylinder boundary). The correct asymptotic convergence at very high curvature is also achieved since for very small diameters (high curvatures) of the cylinder, mass transfer rate will be suppressed to the wall (lower curved surface area is present). This has been confirmed by Gebhart *et al.* [77] and Evans [78]. Scrutiny of **Fig. 16** reveals that the local Sherwood number for species A exhibits a warped topology. Increasing Schmidt number depletes the $Sh_{x,\ A}$ magnitudes, as does increasing curvature parameter. Maximum $Sh_{x,A}$ magnitudes are computed for minimal Schmidt number and zero cylinder curvature (top left of contour plot) whereas the opposite scenario is observed at high Schmidt number and maximum curvature (bottom right back corner of the plot). The *non-linearity* in interplay between curvature and Schmidt number is clearly captured in this plot and both exert a profound influence on species diffusion towards the cylinder surface. Fig. 17 also shows that a skewed topology is computed for $Sh_{x,A}$ magnitudes with simultaneous variation in cylinder curvature parameter (γ) and homogenous reaction parameter (K). The contours are warped towards the front left top corner. Maximum local Sherwood number for species A arises for zero curvature and highest homogenous reaction parameter values. Minimum local Sherwood number for species A is computed in the back lower right corner and corresponds to maximum cylinder curvature and the lowest value of homogenous reaction parameter. A steady topology is computed with no sudden dips or crests.

Figs. 18 - 21 provide visualizations of computations for species B (hydrogen) characteristics. **Fig. 18** depicts the response in species B concentration profiles $h(\eta)$ with transverse

coordinate (η) for (a) Schmidt number, (b) heterogenous reaction parameter, (c) curvature parameter and (d) homogenous reaction parameter. A separate species boundary layer Eqn. (15) describes the mass transport of species B (hydrogen) in the nano-polymer. This equation has a very similar structure to the species A concentration boundary layer equation (14) with the exception of the homogenous reactive term, which, as identified earlier, is negative in the case of species A whereas it is positive in the case of species B. This has a dramatic influence on the transverse variation of species B concentration, $h(\eta)$ compared to species A concentration $g(\eta)$ over exactly the same range of parameters studied (compare with Figs. 6a-d). Increasing Schmidt number (fig. 18a) generates a marked reduction in species B concentration magnitudes (whereas species A, fig. 6a produces an increase). Larger mass (molecular) diffusivity of species B i.e. D_B, relative to the constant nano-polymer momentum diffusivity, is counter-productive whereas larger species diffusivity of species A i.e. D_A is assistive. The trend in fig. 18a is sustained at all locations in the boundary layer transverse to the cylinder surface. Maximum magnitudes of species B concentration, $h(\eta)$, consistently occur at the cylinder surface irrespective of the Schmidt number. With increasing heterogenous reaction parameter, Ks (fig. 18b) there is a noticeable upsurge in species B concentration. Asymptotically smooth decays are computed for all cases from the cylinder surface to the free stream. Conversely a marked suppression in species B concentration is observed with increasing curvature parameter (fig. 18c). Diffusion of species B (hydrogen) is therefore encouraged in the coating boundary layer regime with stronger boundary reaction effect whereas it is inhibited with greater curvature (smaller diameter) - these patterns are opposite to those reported in figs. 6b,c for species A concentration. Finally, fig. 18d indicates that an *acute elevation* in species B concentration is induced with greater homogenous chemical reaction parameter (contrary to the *decrement in species A*, fig 6d). Again, it is noteworthy that since the sum of species A and B concentrations equals unity (as per the condition given in Eqn. (19)) an increment in one species must be accompanied by a decrement in the other and vice versa. This is the nature of bulk homogenous reaction of first order for dual species where a catalytic boundary reaction at the substrate surface is also present. **Fig. 19** depicts the evolution in local Sherwood number, $Sh_{x,B}$. for Species B with various parameters. The contour topologies associated with Fig. 19 are subsequently visualized in Figs. 20 and 21. The patterns computed are the exact opposite of those for species A in Fig. 15. Fig. 19a shows that an increment in Schmidt number induces a considerable enhancement in local Sherwood number, $Sh_{x,B}$. Furthermore there is a significant elevation in $Sh_{x,B}$. with increasing cylinder curvature

for $Sc = 1$ (momentum and species B concentration boundary layer thicknesses are the same). However at higher Schmidt numbers while there is an increment in $Sh_{x,B}$ the relationship with increasing curvature parameter is linear and becomes progressively weaker. Fig. 19b shows that $Sh_{x,B}$ magnitudes are reduced substantially at any value of curvature parameter with increasing homogenous reaction parameter. However, with increasing curvature parameter there is a sustained monotonic growth in local Sherwood numbers. Overall, it may deduced that, with increasing strength of first order homogenous chemical reaction parameter, K, mass transfer rate of species B to the cylinder surface is supressed whereas mass transfer rate of species A to the boundary is encouraged (fig. 15b). The contour plot for species B local Sherwood number versus Schmidt number and curvature parameter (**Fig. 20**) shows a staggered topology; maximum $Sh_{x,B}$ arises at maximum curvature (γ) and maximum Schmidt number (Sc = 3) in the top back corner of the plot. Minimum $Sh_{x,B}$ however surfaces at zero curvature and minimal Schmidt number ($Sc = 1$) at the bottom left corner (front) of the contour plot. Again, there is a noticeable skewness in the topology, although on this occasion it is towards the back lower corner, whereas for species A (fig. 16) it is located at the top right front corner. **Fig. 21** displays the contour plot for species B local Sherwood number $Sh_{x,B}$ versus homogenous reaction parameter and curvature parameter. Generally, a monotonic topology from the front lower zone to the back upper zone is computed, which is significantly different from that for species A local Sherwood number in fig. 17. Maximum $Sh_{x,B}$ arises at maximum value of curvature for any value of homogenous chemical reaction parameter (dark red contours at back of plot). Minimal $Sh_{x,B}$ arises at the minimal value of cylinder curvature parameter, specifically zero curvature (flat substrate); however there is a linear decay with increasing homogenous chemical reaction parameter, *K, and higher $Sh_{x,B}$* occurs for $K = 1$ compared with $K = 3$, for *any value* of curvature parameter (γ). As emphasized earlier, there is a strong interplay between Schmidt number, curvature and first order homogenous chemical reaction parameters in determining the effective magnitude of the local Sherwood numbers of both species A and B. Specifically it may be emphasized that the molecular diffusivity of the diffusing reactive species (oxygen, hydrogen) and other properties of the functional nano-polymer can be manipulated to orchestrate different responses in the transport phenomena. An increase in dynamic viscosity of the functional coating material (nano-polymer) will increase Schmidt number, whereas an increase in density of nano-polymer or molecular (mass) diffusivity of the species (A, B) will reduce Schmidt number. Of course, more species may be considered in

more complex chemical synthesis and deposition processes and these can be examined in the future.

6. CONCLUSIONS

Stimulated by providing a deeper insight into the coating fluid dynamics of novel functional magnetic nano-polymers, of potential interest in aerospace, nuclear, marine and medical engineering, a novel mathematical model has been presented for dual catalytic reactive species diffusion in axisymmetric coating enrobing forced convection boundary layer flow from a linearly axially stretching horizontal cylinder. The cylinder (substrate) is immersed in a homogenous non-Darcy porous medium saturated with the functional nano-polymer. Homogeneous and heterogeneous reactions, heat source (e.g. laser source) and non-linear radiative transfer (Rosseland's diffusion flux model) are included. The Tiwari-Das nanoscale model is deployed. A Darcy-Forchheimer drag force formulation is utilized to simulate both bulk porous drag and second order inertial drag of the porous medium fibres. The magnetic nano-polymer is an aqueous "functional" electro conductive polymer (ECP) comprising base fluid water and magnetic TiO_2 nanoparticles. Viscous heating and Ohmic dissipation are also included to produce a more physically realistic thermal analysis. The non-linear conservation equations for mass, momentum, energy and species diffusion (species A and B) are transformed via an appropriate stream function and scaling variables into a system of non-linear coupled multi-degree ordinary differential equations (ODEs). The emerging nonlinear ordinary differential boundary value problem is solved with four-point Gauss-Lobatto formulae in the MATLAB bvp5c routine. Verification of the MATLAB bvp5c computations has been achieved with an efficient, rapidly convergent and robust Adams-Moulton predictor-corrector numerical scheme (AM2). A comprehensive study of the impact of key thermophysical, electromagnetic, nanoscale and geometric parameters has been conducted. Extensive visualization of velocity, temperature, species A concentration, species B concentration, skin friction, local Nusselt number and species A and B local Sherwood numbers has been provided. The main findings from the present simulations may be summarized as follows:

(i)   Axial flow is retarded with higher volume fraction (since the viscosity of the nano-coating is elevated) and also reduced with Stuart magnetic interaction number. With increasing Forchheimer quadratic drag parameter, there is also a marked decrease in the axial velocity. In all these cases momentum (hydrodynamic) boundary layer thickness is increased in the nano-polymer coating.

(ii) With increasing Darcian parameter (higher pemeability) there is less resistance to the nano-polymer offered by porous matrix which induces *axial flow acceleration*. Higher curvature parameter also produces *strong axial flow acceleration*

(iii) Increasing volume fraction of Titanium dioxide nanoparticles reduces temperatures within the coating layer, since it encourages heat diffusion to the wall. Increasing curvature parameter also increases temperatures as does higher Stuart magnetic interaction parameter and Ohmic dissipation i.e. Joule electrical heating. However, with higher Darcy parameter the temperature (and thermal boundary layer thickness) is reduced in the regime due to the decrease in thermal conduction with a depletion in solid fibres. Higher Eckert number, *Ec,* which corresponds to greater viscous heating effect in the nano-polymer, boosts temperature and also thermal boundary layer thickness of the nano-polymer coating. Therefore omission of this effect in functional magnetic nano-coating models under-predicts temperatures in the boundary layer i.e. less accuracy in characterizing thermal distribution. Higher Prandtl number however manifests in a strong reduction in temperature distribution (owing to the inverse proportionality to effective thermal conductivity of the magnetic nano-polymer). Higher values of radiation-conduction (Boltzmann) number, *Nr,* heats the nano-polymer coating regime substantially and boosts thermal boundary layer thickness. Temperatures are also accentuated with greater temperature ratio parameter and heat source (e.g. laser thermal loading).

(iv) Surface skin friction is elevated with greater magnetic interaction parameter (Stuart number) and similarly there is a boost in skin friction (at the substrate interface with the coating) with increasing Titanium dioxide nanoparticle volume fraction. With greater Darcy parameter (higher permeability i.e. a more sparsely packed porous matrix) there is an enhancement in skin friction. However, despite the greater inertial contribution with higher Forchheimer quadratic drag parameter, the flow is decelerated at the wall i.e. skin friction magnitudes are reduced. A similar reduction in skin friction is induced with greater cylinder curvature (smaller diameter cylinders).

(v) Nusselt number is significantly decreased with greater magnetic interaction parameter i.e. cooling of the metal substrate (cylinder) is produced. Nusselt number is also depleted with increasing Eckert (viscous heating) number, Ohmic dissipation and temperature ratio, since both these quantities are known to *heat* the boundary layer coating. This increases the *heat transferred away from the cylinder* to the

nano-polymer and results in a simultaneous decrease in heat transferred to the cylinder. Furthermore, with greater heat source effect Nusselt number is also suppressed since the body of the nano-polymer is heated (temperatures increased) and heat migrates away from the wall, not towards the wall. Conversely with increasing Prandtl number, since the nano-polymer is cooled, heat is successfully conveyed to the cylinder surface i.e. Nusselt number magnitudes are enhanced. Higher radiative-conduction parameter (Boltzmann number) energizes the nano-polymer and boosts local Nusselt numbers.

(vi) With increment in Schmidt number and curvature parameter, there is a significant increase in species *A* concentration (molecular oxygen) magnitudes whereas the opposite effect is induced with larger homogenous (bulk polymer reaction) and heterogenous reaction parameters (boundary reaction due to autocatalysis at the cylinder surface), since species *A* (oxygen) is converted by these destructive reactions. The opposite effects are induced in species *B* (hydrogen) concentration magnitudes.

(vii) With increasing Schmidt number and curvature parameter there a strong depletion in local Sherwood number (convective mass transfer rate of species *A* to the wall). The contour plots for local Sherwood number for species A exhibit a warped topology. Maximum species A local Sherwood number magnitudes are observed for minimal Schmidt number and zero-cylinder curvature whereas the opposite scenario is computed at high Schmidt number and maximum curvature. Local Sherwood number for species B is elevated with an increment in Schmidt number and increasing curvature parameter whereas it is depreciated with increasing homogenous reaction parameter. Effectively, with increasing strength of first order homogenous chemical reaction (bulk reaction), mass transfer rate of species *B* to the cylinder surface is supressed whereas mass transfer rate of species A to the boundary is encouraged (fig. 15b). Various anomalies in the topologies of the local Sherwood number are also identified.

The present study has revealed some interesting characteristics of functional (magnetic) nano-polymer reactive coating flows. MATLAB BVP5C shooting quadrature and Adams-Moulton predictor corrector methods have proved to be very efficient numerical tools for solving the complex coupled nonlinear differential equations describing the axisymmetric coating regime for a stretching cylinder substrate. However, magnetization (magnetic dipole), ferroelectric and piezoelectric effects have been neglected. These require ferrohydrodynamic theory [79], ferro-

electro-mechanical models [80] for modelling e.g. lead-magnesium-niobate (PbMgN) and piezo-electric fluid-solid models [81] for simulating e.g. lead zirconate titanate (PZT), and polymers, such as polyvinylidene flouride (PVDF), which generate a stress in response to an applied voltage (rather than an external magnetic field as considered in the present study). Efforts in this direction are underway and will be communicated, in the near future.

REFERENCES

[1] Kung-ChinChang and Jui-MingYeh, Chapter 16 - Electroactive Polymer-Based Anticorrosive Coatings, in *Intelligent Coatings for Corrosion Control, Eds. Atul Tiwari, James Rawlins and Lloyd H. Hihara,* 557-583, Butterworth-Heinemann, USA (2014).

[2] MD. Shamshuddin, S.R. Mishra, O. Anwar Bég, T.A. Bég and Ali Kadir, Computation of radiative Marangoni (thermocapillary) magnetohydrodynamic convection in Cu-water based nanofluid flow from a disk in porous media: smart coating simulation, *Heat Transfer (2020). DOI: 10.1002/htj.21963 (20 pages)*

[3] https://www.intelligentmaterial.com/ IMS' Intelligent Material® (2020).

[4] D. E. Weidner, Maximum sustainable volume of a magnetic fluid coating a horizontal cylinder carrying an axial electric current, *J. Magnetism and Magnetic Materials,* 489, 165352 (2019).

[5] W. Chen *et al.,* Magnetic hydroxyapatite coatings with oriented nanorod arrays: hydrothermal synthesis, structure and biocompatibility, *J. Mater. Chem. B*, 2, 1653-1660 (2014).

[6] F. Xia *et al.,* Synthesis of Ni–TiN composite nanocoatings by magnetic pulse current deposition, *Ceramics International: A*, 41 (9) 11445-11448 (2015).

[7] T. Cheng et al, Magnetic particle-based super-hydrophobic coatings with excellent anti-icing and thermo-responsive de-icing performance, *J. Mater. Chem. A*, 3, 21637-21646 (2015).

[8] S. H. Teh and I. I. Yaacob, Synthesis and characterization of Co-Fe nanocrystalline magnetic films electrodeposited from electrolyte solution containing sodium saccharin, *IEEE Transactions on Magnetics*, 47 (10) 4398–4401 (2011).

[9] K. M. Hyie *et al.,* The physical and magnetic properties of electrodeposited Co-Fe nanocoating with different deposition times, *Journal of Nanomaterials,* Article ID 680491, 10 pages (2013).

[10] Gurrappa and L. Binder, Electrodeposition of nanostructured coatings and their characterization—a review, *Science and Technology of Advanced Materials*, 9 (4) Article ID 043001, 11 (2008).

[11] Halim, J, Abdel-karim, R, Raghy, S, Nabil, M, & Waheed, A. Electrodeposition and characterization of nanocrystalline Ni-Mo catalysts for hydrogen production. *J. Nanomaterials* 2012, Article ID 845673, 10 pages (2012).

[12] Tang, T.; Fu, Y. Formation of chitosan/sodium phytate/nano-Fe_3O_4 magnetic coatings on wood surfaces via layer-by-layer self-assembly. *Coatings, 10*, 51 (2020).

[13] Wang, H.; Chen, T.; Cong, W.; Liu, D. Laser cladding of Ti-based ceramic coatings on Ti6Al4V alloy: Effects of CeO_2 nanoparticles additive on wear performance. *Coatings, 9*, 109 (2019).

[14] S. Vorobyev *et al.,* Reactivity and chemical sintering of Carey Lea Silver nanoparticles, *Nanomaterials,* 9(11), 1525 (2019).

[15] He, D.; Grag, S.; Waite, T.D. H_2O_2-mediated oxidation of zero-valent silver and resultant interactions among silver nanoparticles, silver ions, and reactive oxygen species. *Langmuir, 28*, 10266–10275 (2012).

[16] Feng, L.; Gao, G.; Huang, P.; Wang, X.; Zhang, C.; Zhang, J.; Guo, S.; Cui, D. Preparation of Pt-Ag alloy nano-island/graphene hybrid composites and its high stability and catalytic activity in methanol electro-oxidation. *Nanoscale Res. Lett., 6*, 551 (2011).

[17] Murr L.E. Synthesis and Processing of Nanomaterials. In: *Handbook of Materials Structures, Properties, Processing and Performance*. Springer, USA (2015).

[18] Kumar M, Ando Y, Chemical vapor deposition of carbon nanotubes: a review on growth mechanisms and mass production. *J. Nanosci. Nanotechnol.*, 10:3739–3758 (2010).

[19] https://www.ssnano.com/ (2020) [SkySpring Nanomaterials, Houston, Texas, USA]

[20] Das, S.K.; Choi, S.U.; Yu, W.; Pradeep, T. *Nanofluids: Science and Technology*; John Wiley & Sons: Hoboken, NJ, USA (2007).

[21] Jafari, R.; Mobarakeh, L.F.; Farzaneh, M. Water-repellency enhancement of nanostructured plasma-polymerized HMDSO coatings using Grey-based Taguchi method. *Nano Sci. Technol. Lett. 4*, 369–374 (2012).

[22] W. Jiang *et al.*, Wear resistance of Ni-Co/SiC composite coating by jet electrodeposition in the presence of magnetic field, *Proc. IMechE- Part B: Journal of Engineering Manufacture*, 234, 431-438 (2019).

[23] M. Tajbakhsh *et al.,* Investigation of the physical and mechanical properties of Ni–P and Ni–P–PTFE nanocomposite coatings deposited on aluminum alloy 7023, *Proc. IMechE- Part E: Journal of Process Mechanical Engineering*, 233, 94-103 (2017).

[24] D. Setti *et al,* Influence of nanofluid application on wheel wear, coefficient of friction and redeposition phenomenon in surface grinding of Ti-6Al-4V, *Proc. IMechE- Part B: Journal of Engineering Manufacture*, 232, 128-140 (2016).

[25] R. K. Tiwari and M. K. Das**,** Heat transfer augmentation in a two-sided lid-driven differentially heated square cavity utilizing nanofluids, *International Journal of Heat and Mass Transfer,* 50, 2002–2018 (2007).

[26] J. Buongiorno, Convective transport in nanofluids, *ASME J. Heat Transfer*, 128, 240-250, (2006).

[27] Koo J. Computational nanofluid flow and heat transfer analyses applied to microsystems. *Ph.D. Thesis, NC State University, Raleigh, NC, USA* (2004).

[28] Li J. Computational analysis of nanofluid flow in micro channels with applications to micro-heat sinks and bio-MEMS. *Ph.D. Thesis, NC State University, Raleigh, NC, USA* (2008).

[29] O. Anwar Bég, A. Subba Rao, N. Nagendra, CH. Amanulla, M. Surya Narayana Reddy and A. Kadir, Numerical study of hydromagnetic non-Newtonian nanofluid transport phenomena from a horizontal cylinder with thermal slip: aerospace nanomaterial enrobing simulation, *J. Nanofluids,* 7, 1–14 (2018).

[30] N. Shukla, P. Rana, O. Anwar Bég, Bani Singh and A. Kadir, Homotopy study of magnetohydrodynamic mixed convection nanofluid multiple slip flow and heat transfer from a vertical cylinder with entropy generation, *Propulsion and Power Research* (2019). https://doi.org/10.1016/j.jppr.2019.01.005 (16 pages)

[31] Bergman, T.L. and Viskanta, R.: Radiation heat transfer in manufacturing and materials processing, in *Radiative Transfer-I, M.P. Menguc, Editor*, pp. 13–39, Begell House, New York, USA (1996).

[32] Viskanta R. Radiation heat transfer in materials processing and manufacturing. *In: Bejan A., Vadász P., Kröger D.G. (eds) Energy and the Environment. Environmental Science and Technology Library*, vol 15. Springer, Dordrecht, Germany (1999).

[33] V. Rajesh, O. Anwar Bég and M. P. Mallesh, Transient nanofluid flow and heat transfer from a moving vertical cylinder in the presence of thermal radiation: Numerical study, *Proc. IMECHE- Part N: J. Nanoengineering and Nanosystems,* 230, 3-16 (2016).

[34] M. J. Uddin, O. Anwar Bég and N. Amin, Hydromagnetic transport phenomena from a stretching or shrinking nonlinear nanomaterial sheet with Navier slip and convective heating: A model for bio-nano-materials processing, *Journal of Magnetism and Magnetic Materials, 368,* 252-261 (2014).

[35] M Ferdows, MS Khan, O. Anwar Bég, MAK Azad, MM Alam, Numerical study of transient magnetohydrodynamic radiative free convection nanofluid flow from a stretching permeable surface, *Proc. IMechE-Part E: J. Process Mechanical Engineering,* 228 (3) 181-196 (2014).

[36] L. Preziosi and D. D. Joseph, The run-off condition for coating and rimming flows, *J. Fluid. Mech.* 187, 99-113 (1988).

[37] V.R. Prasad, A. SubbaRao, N. Bhaskar Reddy, B. Vasu, O. Anwar Bég, Modelling laminar transport phenomena in a Casson rheological fluid from a horizontal circular cylinder with partial slip, *Proc IMechE- Part E: J. Process Mechanical Engineering,* 227 (4) 309-326 (2013).

[38] D. E. Weidner, L. W. Schwartz, and M. H. Eres, Simulation of coating layer evolution and drop formation on horizontal cylinders, *J. Colloid Interface Sci.* 187, 243 (1997).

[39] V. Ramachandra Prasad, S. Abdul Gaffar, E. Keshava Reddy, and O. Anwar Bég, Flow and heat transfer of Jefferys non-Newtonian fluid from a horizontal circular cylinder, *AIAA J. Thermophysics and Heat Transfer,* 28, 764-770 (2014).

[40] D.E. Weidner, Drop formation in a magnetic fluid coating a horizontal cylinder carrying an axial electric current, *Physics of Fluids*, 29, 052103 (2017

[41] G. Janardhana Reddy, Bhaskerreddy Kethireddy and O. Anwar Bég, Flow visualization using heat lines for unsteady radiative hydromagnetic micropolar convection from a vertical slender hollow cylinder, *Int. J Mechanical Sciences,* 140, 493-505 (2018).

[42] Bilal M., Sagheer M., Hussain S., Mehmood Y., MHD stagnation point flow of Williamson fluid over a stretching cylinder with variable thermal conductivity and homogeneous or heterogeneous reaction. *Communications in Theoretical Physics*, 67(6): 688-695 92017).

[43] A. Kumar and P. M. Kumar, Boundary layer flow and heat transfer analysis on Cu-water nanofluid flow over a stretching cylinder with slip, *Alexandria Engineering Journal, 56 (4)* 671-677 (2017).

[44] A. Zaib et al, Impact of homogeneous–heterogeneous reactions on mixed convection flow of a copper–water nanofluid past a permeable shrinking cylinder with thermal radiation, *Proc. IMechE- Part E: Journal of Process Mechanical Engineering*, 232 (5) 566-578 (2017).

[45] A. Mahdy, Entropy generation of tangent hyperbolic nanofluid flow past a stretched permeable cylinder: Variable wall temperature, *Proc. IMechE- Part E: Journal of Process Mechanical Engineering*, 233 (3) 570-580 (2018).

[45] MD. Shamshuddin, M. Ferdows, Rezwan, O. Anwar Bég, A. Kadir, Ferromagnetic and non-magnetic nanoparticles in nanofluid flow from a stretching cylinder with magnetic induction: spectral relaxation solution, *Proceedings of the International Conference on Numerical Heat Transfer and Fluid Flow (NHTFF-2020), NIT Warangal, India – Jan 17-19* (2020).

[47] Hashim *et al.,* Characteristics of melting heat transfer during flow of Carreau fluid induced by a stretching cylinder, *The European Physical Journal E,* 40, Article number: 8 (2017).

[48] D. Kawale *et al.,* Polymer conformation during flow in porous media, *Soft Matter*, 13, 8745 (2017).
[49] Ishizaki K., Komarneni S., Nanko M., Applications of porous materials. In: *Porous Materials. Materials Technology Series*, vol 4. Springer, Boston, USA (1998).

[50] S. Kang *et al.,* Mechanism of heat transfer through porous media of inorganic intumescent coating in cone calorimeter testing, *Polymers,* 11(2): 221 (2019).

[51] K. Vafai and C.L. Tien, Boundary and inertia effects on convective mass transfer in porous media, *Int. J. Heat Mass Transfer*. 25 (8) 1183-1190 (1980).

[52] A. Dybbs and R. V. Edwards, A new look at porous media fluid mechanics — Darcy to turbulent, *Fundamentals of Transport Phenomena in Porous Media* pp 199-256, Ed. J. Bear, NATO Series, Netherlands (1984).

[53] Joseph, D.D., Nield, D.A. and Papnicolaou, G., Nonlinear equation governing flow in a saturated porous medium, *Water Resources Research*, 18, 1049-1052 (1982).

[54] Lage, J.L., The fundamental theory of flow through permeable media from Darcy to turbulence, *D.B. Ingham and Pop, I., (editors), Transport Phenomena in Porous Media*, Elsevier Science, Oxford, 1-30 (1998).

[55] Skejtne, E. and Auriault, J.L., New insights on steady, nonlinear flow in porous media, *Eur J. Mechanics B: Fluids*, 18, 131-145 (1999).

[56] J. Zueco, O. Anwar Bég, Tasveer A. Bég and H.S. Takhar, Numerical study of chemically-reactive buoyancy-driven heat and mass transfer across a horizontal cylinder in a high-porosity non-Darcian regime, *J. Porous Media*,12, 6, 519-535 (2009).

[57] O. Anwar Bég, Bakier, A.Y. and V.R. Prasad, Numerical study of free convection magnetohydrodynamic heat and mass transfer from a stretching surface to a saturated porous medium with Soret and Dufour effects, *Computational Materials Science*, 46, 1, 57-65 (2009).

[58] Md Faisal Md Basir, M.J. Uddin, A. I. Md. Ismail and O. Anwar Bég, Unsteady bio-nanofluid slip flow over a stretching cylinder with bioconvection Schmidt and Péclet number effects, *AIP Advances,* 6, 055316-1 - 055316-15 (2016).

[59] Barik A K, Mishra S K, Mishra S R and Pattnaik P K, Multiple slip effects on MHD nanofluid flow over an inclined, radiative and chemically reacting stretching sheet by means of FDM, *Heat Transfer, 47,* 1–25 (2019).

[60] Mishra S R, Pattnaik P K, Bhatti M M, Abbas T, Analysis of heat and mass transfer with MHD and chemical reaction effects on viscoelastic fluid over a stretching sheet, *Indian Journal of Physics*, 91 (10) 1219-1227 (2017).

[61] O. Anwar Bég, S. Kuharat, M. Ferdows, M. Das, A. Kadir, M. Shamshuddin, Magnetic nano-polymer flow with magnetic induction and nanoparticle solid volume fraction effects: *solar magnetic nano-polymer fabrication simulation, Proc. IMechE-Part N: J Nanoengineering, Nanomaterials and Nano-systems* (2019). DOI: 10.1177/ 2397791419838714 (19 pages)

[62] Pattnaik P K, Mishra S R, Bhatti M M, Duan–Rach approach to study Al_2O_3-Ethylene Glycol $C_2H_6O_2$ nanofluid flow based upon KKL model, *Inventions,* 5, 45 (2020).

[63] S. Mansur et al., Stagnation-point flow towards a stretching/shrinking sheet in a nanofluid using Buongiorno's model, *Proc. IMechE- Part E: Journal of Process Mechanical Engineering*, 231 (2) 172-180 (2015).

[64] M. Van Elsen *et al.,* Solutions for modelling moving heat sources in a semi-infinite medium and applications to laser material processing, *International Journal of Heat and Mass Transfer*, 50, 23/24, 4872-4882 (2007).

[65] S.L. Chen, Analysis and modelling of reactive three-dimensional high-power CO_2 laser cutting, *Proc. IMechE. - Part B: Journal of Engineering Manufacture*, 212 (2) 113-128 (1998).

[66] B.S. Yilbas, *Laser Heating Applications*, Elsevier, USA (2012).

[67] Bég, O. Anwar, Numerical methods for multi-physical magnetohydrodynamics, *J. Magnetohydrodynamics and Plasma Research*, 18, 2, 93-200 (2013).

[68] Shampine, L.F., and J. Kierzenka, A BVP solver that controls residual and error (MATLAB bvp5c), *J. Numer. Anal. Ind. Appl. Math.* 3(1/2), 27–41 (2008).

[69] S. Pal, *Numerical Methods: Principles, Analyses and Algorithms*, Oxford University Press, India (2009).

[70] O. Anwar Bég, J. Zueco, H. S. Takhar, T. A. Bég and A. Sajid, Transient non-linear optically-thick radiative-convective double-diffusive boundary layers in a Darcian porous medium adjacent to an impulsively started surface: network simulation solutions, *Communications in Nonlinear Science and Numerical Simulation*, 14, 3856-3866 (2009).

[71] S. Qayyum *et al.,* A framework for nonlinear thermal radiation and homogeneous/heterogeneous reactions flow based on silver-water and copper-water nanoparticles: A numerical model for probable error, *Results in Physics*, 7 (2017) 1907–1914 (2017).

[72] R.D. Russell and J. Christiansen, Adaptive mesh selection strategies for solving boundary value problems, *SIAM J. Numer. Anal*., 14, 59–80 (1978).

[73] R. Chanda *et al*., Heat and mass transfer properties of zeolite coatings: comparison of reactive- and spray-coated systems, *Journal of Thermal Spray Technology*, 28, 4, 598-644 (2019).

[74] F.P. Incropera and D.P. De Witt, *Fundamentals of Heat and Mass Transfer*, 5th edn, John Wiley & Sons, New York, USA (2001).

[75] E. Petrovicova and L. S. Schadler, Thermal spraying of polymers, *International Materials Reviews*, 47, 169-190 (2002).

[76] R. V. Roy and L. W. Schwartz, Coating flows over curved substrates, *Fluid Mechanics of Coating Processes, edited by P. Bourgin, Proceedings of the Second European Coating Symposium, Strasbourg, France* (1997).

[77] B. Gebhart, *Heat Conduction and Mass Diffusion*, MacGraw-Hill, New York, USA (1993).

[78] P. L. Evans, Mathematical and numerical investigations of coating flows, *Ph.D. Thesis, University of Delaware*, USA (2000).

[79] R. Rosensweig, *Ferrohydrodynamics*, MIT Press, USA (1985).

[80] N. Mukhin *et al*., Composite ferroelectric coatings based on a heat-resistant polybenzoxazole polymer matrix, *Coatings*, *10*(3), 286 (2020).

[81] M. Chelu *et al.,* High-quality PMMA/ZnO NWs piezoelectric coating on rigid and flexible metallic substrates, *Applied Surface Science*, 529, 147135 (2020).

NOTATION

a	Positive dimensional constant (-)
a_0	Constant (-)
A_1	Ratio of nano-polymer (nanofluid) to base liquid density (-)
A_2	Ratio of nano-polymer (nanofluid) to base liquid dynamic viscosities (-)
A_3	Ratio of nano-polymer (nanofluid) to base liquid electrical conductivity (-)
A_4	Ratio of nano-polymer (nanofluid) to base liquid thermal conductivity (-)
A_5	Ratio of nano-polymer (nanofluid) to base liquid heat capacitance (-)
B_0	Strength of magnetic field (Tesla)
C_{fx}	Axial skin friction coefficient (-)
c_p	Specific heat capacity under isobaric conditions (J/K)
D_A, D_B	Molecular diffusivities for species *A*, *B* (m^2/s)
Ec	Eckert (viscous heating) number (-)
f	Stream function (-)
f'	Dimensionless velocity (-)
g	Dimensionless species A concentration (-)
h	Dimensionless species B concentration (-)
I^*	Forchheimer inertia coefficient (-)
I_f	Dimensionless Forchheimer inertia coefficient (-)
K^*	Permeability (hydraulic conductivity) of porous medium (m^2)
K	Homogenous reaction rate constant (-)
Ks	Heterogenous reaction rate constant (-)
k_{nf}	Thermal conductivity of nano-polymer (W/mK)
k_f	Thermal conductivity of base liquid (aqueous) (W/mK)
k_s	Thermal conductivity of titanium dioxide nanoparticles (W/mK)
k_1	Reaction rate constant (-)
k^*	Mean absorption radiative coefficient (-)
K_1, K_2, K_3, K_4	MATLAB bvp5c numerical approximations (-)

Kp	Darcian parameter (non-dimensional permeability parameter) (-)
l	Characteristic length deployed (length of cylinder) (m)
M	Magnetic interaction (Stuart) number (-)
Nu_x	Local Nusselt number (-)
Nr	Radiation-conduction (Boltzmann) parameter (-)
Pr	Prandtl number (-)
q_r	Radiative radial thermal heat flux (W/m^2)
q_w	Surface heat flux (W/m^2)
$q_{m\,(A)}$	Surface mass flux of species A (Moles/m^2)
$q_{m\,(B)}$	Surface mass flux of species B (Moles/m^2)
r	Radial (transverse) coordinate (m)
Q_0	Dimensional heat source parameter (W/m^3.K)
Re_x	Local Reynolds number (-)
S	Dimensionless heat source parameter (-)
Sc	Schmidt number (-)
$Sh_{x,A}$	Sherwood number for Species A (-)
$Sh_{x,B}$	Sherwood number for Species B (-)
T	Nano-polymer temperature (K)
T_w	Wall (cylinder surface) temperature (K)
T_∞	Ambient temperature (K)
u	Velocity component in x (axial) direction (m/s)
U_w	Constant axial cylinder stretching velocity (m/s)
u_0	Characteristic axial velocity (m/s)
v	Velocity component in r (radial) direction (m/s)
x	Axial coordinate (m)
Y_1	MATLAB bp5c initial guess (-)

Greek Symbols

γ	Cylinder curvature parameter (-)
δ	Ratio of mass diffusivities of species A and B i.e. (D_B/D_A) (-)
ζ	Step distance in MATLAB or Adams-Moulton predictor corrector method (-)

θ	Dimensionless temperature (-)
θ_w	Temperature ratio parameter (-)
η	Dimensionless transverse (radial) coordinate (-)
v_{nf}	Kinematic viscosity of nano-polymer (m^2/s)
μ_{nf}	Dynamic viscosity of nano-polymer (kg/(ms))
μ_f	Dynamic viscosity of base liquid (aqueous) (kg/(ms))
ρ_{nf}	Density of nano-polymer (kg/m^3)
ρ_f	Density of base liquid (aqueous) (kg/m^3)
ρ_s	Density of titanium dioxide nanoparticles (kg/m^3)
$(\rho c_p)_{nf}$	Heat capacitance of nano-polymer (J/K)
$(\rho c_p)_f$	Heat capacitance of base liquid (aqueous) (J/K)
$(\rho c_p)_{nf}$	Heat capacitance of titanium dioxide nanoparticles (J/K)
χ	Concentration of the chemical species A (moles/m^3)
ψ	Concentration of the chemical species B (moles /m^3)
ϕ	Metallic (Titanium) oxide nanoparticle volume fraction (-)
σ_{nf}	Electrical conductivity of nano-polymer (Siemens/m)
σ_f	Electrical conductivity of base liquid (aqueous) (Siemens/m)
σ_s	Electrical conductivity of titanium dioxide nanoparticles (Siemens/m)
$\sigma*$	Stefan-Boltzmann radiation constant (5.670374419×10^{-8} W·m^{-2}·K^{-4})
$\Omega = \dfrac{\sigma_s}{\sigma_f}$	Ratio of nanoparticle to base liquid electrical conductivity (-)
τ_w	Shear stress (N/m^2)

Subscripts

f	Base fluid particles
s	Nanoparticles (solid)
nf	Nanofluid (functional nano-polymer)